Università degli studi di Padova

DIPARTIMENTO DI FISICA E ASTRONOMIA GALILEO GALILEI
Corso di Laurea magistrale in Astronomia

Master Thesis

Radio and near-infrared morphology of NLS1 J0354-1340

Candidate:
Amelia Vietri

Supervisor:
Prof. Stefano Ciroi

Co-Supervisors:
Dr. Emilia Järvelä

Dr. Marco Berton

Academic year 2020-2021

Alle mie guiding lights

A mia madre Franca, a mio padre Roberto, a mia zia Gina

ABSTRACT

Narrow-line Seyfert 1 galaxies (NLS1s) are a peculiar subclass of active galactic nuclei (AGN), characterised by narrow permitted lines ($FWHM(\mathrm{H}\beta) < 2000$ km s^{-1}), a flux ratio of [O III]λ5007/H$\beta < 3$ and often strong Fe II multiplets emission. The narrowness of permitted lines is usually explained as the effect of a low rotational velocity around a low-mass black hole (BH, $M_{\mathrm{BH}} < 10^8\ M_{\odot}$) and since the bolometric luminosity is comparable to that of broad-line Seyfert 1 galaxies, the accretion luminosity is close to the Eddington limit. This property may suggest that NLS1s represent the young evolutionary phase of AGN. Some authors, instead, proposed that the low BH mass of NLS1s is due to an inclination effect, caused by the lack of Doppler broadening due to the pole-on view of a disk-like broad-line region (BLR). Studying host galaxy morphologies can be useful to disentangle these two scenarios since there are relations between the BH mass and properties of its host galaxy bulge. Generally, more massive BHs are found to be hosted in elliptical galaxies while spiral galaxies tend to harbour less massive BH. Until now, only a few studies have focused on NLS1 hosts, finding that these AGN are preferably, but not only, hosted in disk-like galaxies, supporting in this way the low-mass scenario. At the same time, the formation, the evolution, and the interplay with the host galaxy of plasma jets in AGN are still debated. Until recently, powerful relativistic radio jets were found to be hosted only in elliptical galaxies while, several NLS1 galaxies harbouring low-mass BHs, have been detected at γ rays. This proved the presence of fully developed relativistic jets hosted in late-type galaxies, confirming that relativistic jets can be harboured also in spirals. Also, in this case, only a few jetted NLS1s have been studied individually.

In this work, I studied the radio properties, radio and spectral index map, and the host galaxy morphology of the peculiar NLS1 J0354-1340. I found out that this NLS1 is a barred spiral/disk galaxy, harbouring the largest radio jets of two hundred kiloparsec, found to date in an NLS1. These results confirm that NLS1s can be hosted in disk-like galaxies even harbouring powerful relativistic jets. In the first chapter, I will describe the basic structure, the physical properties and the classification of AGN. I will focus in particular on NLS1s. The second part of the thesis is dedicated to radio analysis while the third part will focus on the near-infrared morphology. In the last chapter, I will discuss the results and give conclusions.

CONTENTS

LIST OF FIGURES

LIST OF TABLES

Part I

INTRODUCTION

1 ACTIVE GALACTIC NUCLEI

Active galactic nuclei (AGN) are the most energetic non-transient phenomena in the Universe (Osterbrock and Ferland, 2006). These peculiar objects produce a great amount of energy radiated over the whole electromagnetic spectrum, from radio to γ rays. The AGN are compact, extremely luminous and often most variable at the shortest observed wavelengths. They lie in the nuclear region of galaxies characterised by highly ionised emission lines, not correlated with stellar activity. The central engine is an active supermassive black hole (SMBH), accreting material from its surrounding, that generates photoionising radiation (Beckmann and Shrader, 2012).

1.1 INTRODUCTION

In the early 1900s, astronomers were focused on the study of the galactic nebulae and their emission line spectra. In 1908 from the Lick Observatory, Edward Fath observed NGC 1068, which was thought to be a galactic nebula. He actually obtained the first optical spectrum of an AGN, showing strong emission lines never seen before (Fath, 1909). Since the existence of other galaxies was still debated at that time, this fascinated discovery inspired astronomers in further works. More sources with those features were discovered some years later when Vesto Slipher and Ewind Hubble confirmed the presence of those strong lines in the nuclear spectra of three galactic nebulae: NGC 1068, NGC 4051 and NGC 4151 (Slipher, 1917, Hubble, 1926). Furthermore, another 20 years passed until Carl Seyfert published his work classifying this new kind of object (Seyfert, 1943) for the first time. He obtained the spectra of a selected group of galaxies with high, stellar-like central surface brightness, finding some of them (NGC1086, NGC1275, NGC3516, NCG4051, NGC4151 e NGC7469) dominated by strong high-ionisation emission lines with a wide or a narrow profile (Khachikian and Weedman, 1974). In 1944, Grote Reber detected Cygnus A at 160 MHz, which was the first detection of an AGN at radio frequencies (Reber, 1944). Another pioneering discovery was made by Maarten Schmidt in 1963, who estimated the redshift of 3C 273, $z = 0.158$, realising that this object was placed well beyond our Galaxy (500 Mpc) (Schmidt, 1963). He also confirmed that 3C 273 was almost 100 times more luminous than a normal bright spiral galaxy, showing a powerful jet of 50 kpc (Greenstein and Schmidt, 1964). Since the nature of these sources was not clear and since there were other similar radio detections in those years,

the objects of this kind, due to their stellar-like optical appearance, were named as Quasi-Stellar Radio Sources (Sandage, 1964, Baade and Minkowski, 1982). Showing these sources the same typical spectra with strong emission lines of Seyfert galaxies, it became clear that those barely discovered objects, all belong to a new class: Active Galactic Nuclei (AGN). The nature of the central engine responsible for the production of such an amount of energy and for these peculiar features was still under debate. Woltjer hypothesised that the central engine could be a really massive object residing within 100 pc from the centre. Only after that general relativity theory and the star evolutionary theory were confirmed, it was proved that only black holes (BHs) could be capable of producing such an extraordinary phenomenon (Woltjer, 1964, Salpeter, 1964, Lynden-Bell, 1964, Zel'dovich and Novikov, 1964).

1.2 PHYSICAL PROPERTIES AND STRUCTURE OF AGN

The peculiarity of AGN lies not only in their physical properties but also in the variety of existing types. The differences between all the classes are due to the diverse observational properties. Some AGN exhibit strong emission lines in their spectra for example, while in other spectra, these may be completely absent. Also, the frequency range at which the energy is radiate covers more than 10 orders of magnitude. Despite this, the basic structure is believed to be rather similar for all of them, as shown in Figure 1.

It has long been assumed, that AGN must be powered by accretion onto supermassive black holes (SMBHs) at the dynamical centres of their host galaxies, with a mass in the range of $10^5 \cdot M_\odot$ (NGC4395) to $10^{10} \cdot M_\odot$ (3C 273). The BH is a dense and compact region of spacetime, being able to generate such an intense gravitational field to trap all the matter within it. The event horizon represents the boundary beyond which light and matter falling towards the BH cannot re-emerge from it. Any information regarding an event within the limit horizon cannot be communicated to an outside observer. The event horizon is defined as the effective size of the BH, determined by its mass and called Schwarzschild radius R_S:

$$R_S = \frac{2 \cdot G \cdot M_{BH}}{c^2} \tag{1}$$

Just outside the BH, from a few R_S to some hundreds of R_S, lies the accretion disk, consisting of matter orbiting the central engine. The gravitational attraction generated by the BH causes the particles of the surrounding environment to be arranged in a disk-like structure, due to the conservation of the angular momentum. The friction due to the viscous interactions between the particles leads to the heating of the moving material that becomes plasma and produces a strong

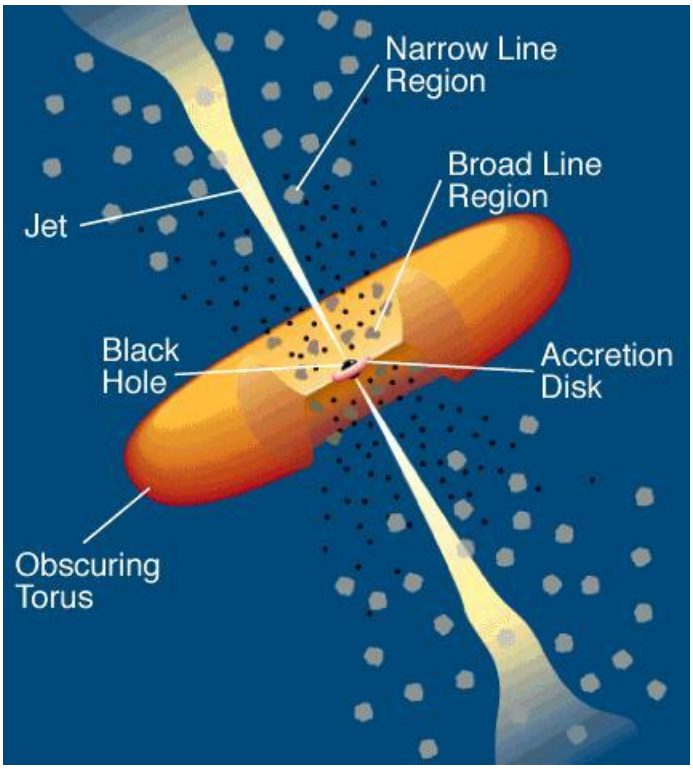

Figure 1: Basic structure of an AGN (Urry and Padovani, 1995).

magnetic field. The conversion of gravitational potential energy into electromagnetic radiation occurs when the material of the disc, accelerating in the magnetic field, produces synchrotron radiation but also optical, UV and X-ray emission. The energy, per unit mass M, available from the conversion is defined as:

$$E = \eta \cdot M \cdot c^2 \tag{2}$$

where η is the efficiency of the conversion and $c = 299792458 m/s$ is the speed of light. The luminosity L emitted from the central region ($L = dE/dt$) defines the rate at which energy is supplied to the nucleus through accretion. The efficiency thus results:

$$\eta = \frac{L_{bol}}{\dot{M} \cdot c^2} \tag{3}$$

having L_{bol} as the bolometric luminosity, $\dot{M}$ as the accretion rate. Considering a spherical symmetric system, the Bondi accretion rate $\dot{M}_B$ is defined as:

$$\dot{M}_B = \frac{4 \cdot \pi \cdot G^2 M_{BH}^2}{V^3} \tag{4}$$

where V is the wind velocity of the escaping particles. The accretion is limited by the radiation pressure effects experienced by

the in-falling plasma. This limit depends on the mass of the compact object and on the mean opacity of the material precipitating on the black hole. The observable quantity corresponding to the critical mass-accretion rate for a source at a known distance is its L, commonly referred to as Eddington luminosity L_{Edd}:

$$L_{Edd} = 3.2 \cdot 10^4 \frac{M_{BH}}{M_\odot} \cdot L_\odot \tag{5}$$

This represents the maximum L a spheroidal system can handle to remain in hydrostatic equilibrium. The Eddington ratio ϵ is defined as the ratio between L_{bol} and L_{Edd} and so the maximum luminosity is reached per $\epsilon = 1$.
There are several models for the physics of the accretion disk, the most relevant three are:

- the radiatively efficient geometrically thin but optically thick disk model (Shakura and Sunyaev, 1976);
- the radiatively inefficient advection dominated accretion flow (ADAF) model (Narayan and Yi, 1994);
- the slim disk model with a disk-like geometry but a significant amount of advection (Mineshige et al., 2000).

Usually, accretion disks are assumed to be standard thin disks, which radiate from optical to soft X-ray band, having a quasi-black body spectrum, with an effective temperature T_{eff} around $10^5 - 10^7$K. The emission from the BH and the accretion disk ionises the outermost compact region of dense gas ($N_e \geqslant 10^9 cm^{-3}$), the broad-line region (BLR). Having an internal radius of around 0.01pc and an external radius of around 0.1pc, BLR is made up of virialised gas clouds orbiting the BH at relatively high speeds ($10^3 - 10^4$km/s). The Doppler broadening due to those rotational velocities is responsible for the broad permitted emission lines, typical of this region, seen in the optical and near-infrared (NIR) spectra. The high density of this region does not allow the formation of forbidden lines. The BLR generally has a $T \approx 10^4$K.
From one to 100 pc lies the tours, an optically thick region made up of dust and molecular clouds with a toroidal shape, surrounding the BLR. These clouds absorb radiation coming from the central engine, obscuring the inner regions when the line of sight falls into it. Only optical emission is absorbed and then re-emitted in infrared (IR), the torus is instead transparent at radio frequencies.
Beyond 100pc, there is a region of very low density gas, $\rho_{NLR} = 10^4 cm^{-3}$, the narrow-line region (NLR). The gas in the NLR is ionised by the radiation coming from the central region, which is responsible for the forbidden and permitted narrow emission lines seen in the

spectra. The narrowness of these lines is due to the lower gas velocity, $v_{NLR} = 10^2 km s^{-1}$, and an electronic density n_e typical of nebular environments, $10^3 cm^{-3} < n_e < 10^6 cm^{-3}$. In some sources the NLR can reach up to few tens of kpc. The distribution of the gas shows a conical or bi-conical shape since it is being ionised by the central continuum, with an opening angle similar to that of the molecular torus (Cracco et al., 2011). This region is called the extended narrow-line region.
Also, some AGN harbour, in addition to the mentioned components, jets launched perpendicularly to the accretion disk and torus plane on both sides. Jets are extremely energetic, highly collimated plasma outflows produced by the accretion disk. They are formed when a fraction of the ionised matter, falling toward the BH, interacts with the magnetic field of the region and is launched away along perpendicular magnetic field lines (Blandford and Znajek, 1977). Some jets can have a size of a few pc, while the most powerful ones ($\approx$ 10% of them) can accelerate to a speed close to c, staying collimated for several kpc, and also reach outside the host galaxy (Mpc-scale jets).
The charged particles, accelerated by the magnetic field, emit non-thermal synchrotron radiation towards the direction they are moving to. The energy distribution of these particles often has a power-law shape, resulting in a power-law shaped observed spectrum with:

$$S \approx \nu^{\alpha} \tag{6}$$

where S is the emitted flux density, ν is the frequency, and α is the power-law index. Synchrotron radiation usually covers from radio to optical/UV bands, depending on the source type. At low frequencies, the emitted synchrotron photons can be re-absorbed by the charged particles that emitted them. This is the synchrotron self-absorption phenomenon that prevents the optically thin synchrotron radiation spectrum from a continuous rise towards the lower frequencies. At higher frequencies, jets emission is produced by the inverse-Compton (IC) mechanism. In IC scattering, photons gain energy from relativistic electrons. The seed photons can originate either from the ambient photon field around the jet (external inverse-Compton) or they can be synchrotron photons produced by the jet itself (synchrotron self-Compton).
Taking into account the relativistic speed of the particles travelling in the jet, when jets point close to our line-of-sight, relativistic effects take place. Apparently, the superluminal motion of the components can be observed and also time dilation effect boosts radiation arriving from a relativistic source. Another effect is the relativistic Doppler boosting that increases radiation travelling towards the observer and diminishes radiation travelling away from the observer. This effect can explain why the approaching jet is brighter than the counter jet.

Finally, the presence of jets in AGN is not strictly related to their radio-loudness R, the ratio between the radio 5 GHz flux density and the optical B-band flux density (Kellermann et al., 1989), despite the jet activity strongly manifesting at radio frequencies. I will discuss this ambiguity in the next section.

1.3 UNIFIED MODEL

A key task in the study of AGN is their classification in the frame of the Unified Model, shown in Figure 2. Over the years, different attempts were made to group several sub-classes of AGN into separate categories until, in 1993, Robert Antonucci unified these attempts by creating a model that takes into account differences in orientation and obscuration (Antonucci, 1993).

For more than 50 years the main classification was related to their radio-loudness: radio-quiet (RQ) and radio-loud (RL) AGN (Sandage, Véron, and Wyndham, 1965), which would show different physical properties, forming two distinct populations. The main difference was in the presence of a powerful relativistic jet in RL AGN and the lack of it in RQ sources (Wilson and Colbert, 1995). Nevertheless, the radio loudness parameter does not really predict the presence of jets of plasma in an AGN, except in extreme cases.
For this reason, taking into account the unreliability of R, it was proposed to group sources for their actual physical property, that is, whether the object shows a powerful relativistic jet or not (Padovani, 2017). These new two typologies are shown in Figure 3. Approximately $\approx$ 90% of AGN do not host relativistic jets and, even if it is possible that these sources harbour less powerful, non-relativistic jets, the jet activity is not dominant as in jetted sources. Considering this classification and, based on spectroscopic differences, there are two main classes of non-jetted AGN: Sefeyrt galaxies and quasars.
Seyfert galaxies represent the most common kind of AGN in the local Universe. Their nucleus is identifiable with that of quasars, radio sources showing bright, central, point-like core and highly ionised emission lines. Today, it is clear that these two classes are similar and the different classification is only due to a selection effect (Leipski et al., 2006). Quasars are identified as brighter objects ($M_b < -21.5 + 5\log h_0$), visible at large distances while, Seyfert galaxies, that are fainter ($M_b > -21.5 + 5\log h_0$), they are only observable at shorter distances (Schmidt and Green, 1983).

Observationally, the main difference among the non-jetted AGN stays in the obscuration of the central engine, caused by the orientation of the AGN relative to the observer. In this way, Type 1 AGN are seen face-on at small inclination angles, the line of sight does

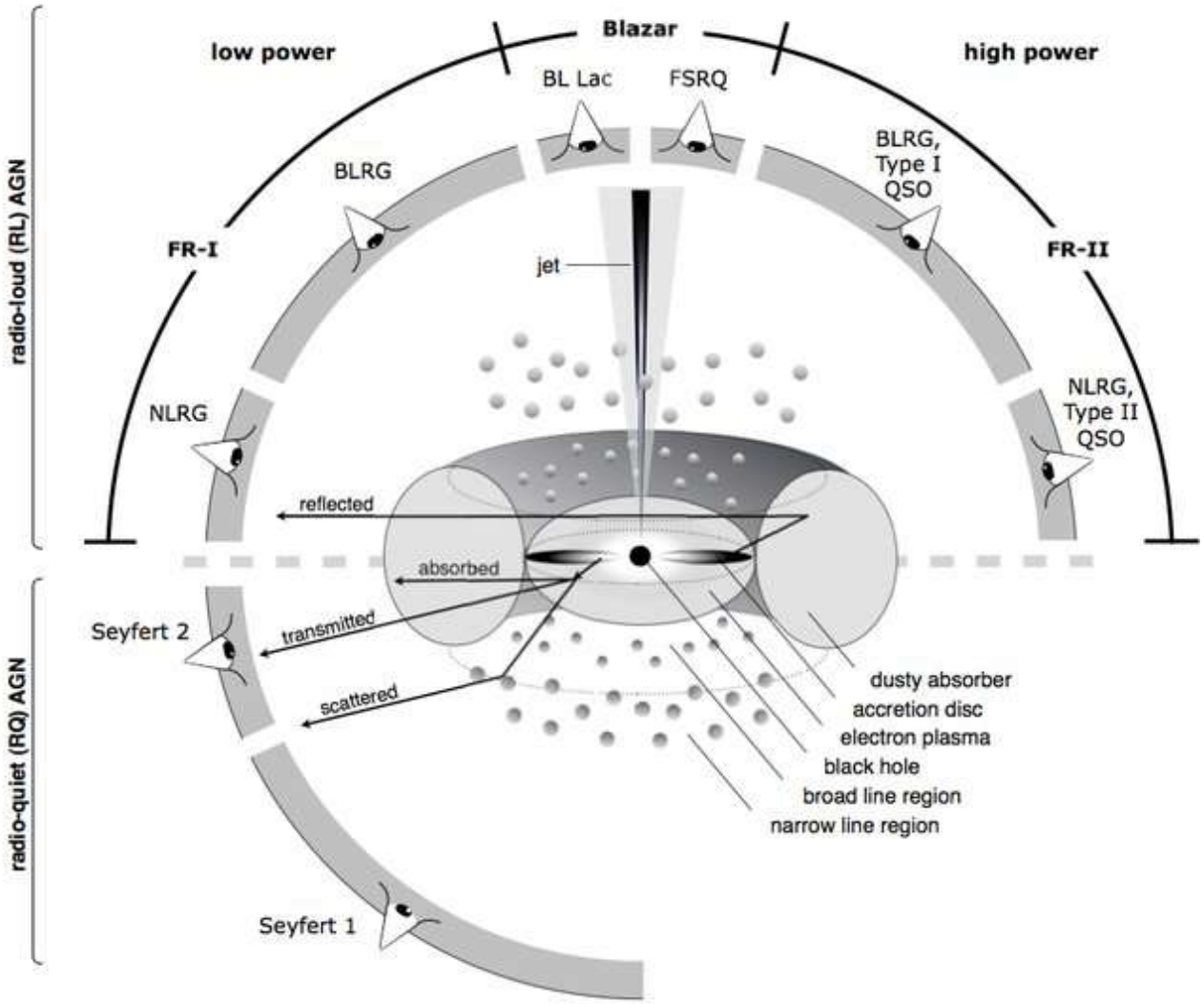

Figure 2: The Unified Model of AGN (Beckmann and Shrader, 2012).

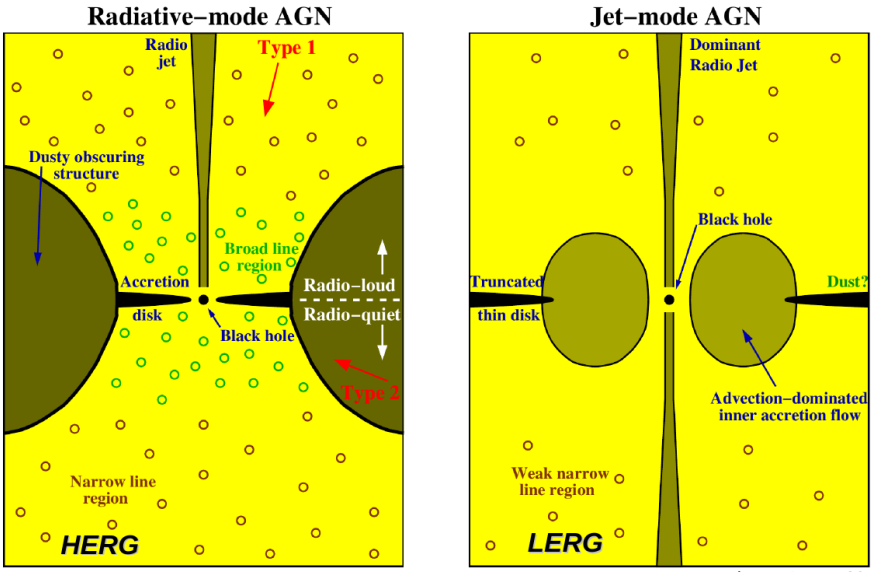

Figure 3: Radiative-mode and jet-mode in AGN (Heckman and Best, 2014).

not fall into the torus and so the central region of the AGN is visible to the observer. The optical spectra of these sources exhibit both broad emission lines arising from the BLR and narrow emission lines coming from the NLR. When the inclination increases, the torus gradually obscures the view of the inner region and the intensity of the broad emission lines decreases. When the torus completely hides the nuclear region, the optical spectra show only narrow lines originating in NLR: these are Type 2 AGN. The Unified Model is based on Type1/Type2 dichotomy. It has also been observed that Type 1 sources are brighter and commonly show a thermal excess in the UV, while in Type 2, the continuum originating in the disc is not visible and the contribution of the host galaxy is predominant.

Optical spectra of Seyfert galaxies exhibit both recombination lines and forbidden lines with a high degree of ionisation so, according to this classification, the difference between Seyfert 1 (Sy1) and Seyfert 2 (Sy2) is caused by the presence or the lack of broad permitted lines. Optical spectra of Sy1 galaxies present broad recombination lines (Full Width at Half Maximum, *FWHM*, of $10^3 \mathrm{km s}^{-1}$) of H and He, other permitted lines of heavy ions like Fe II, C IV and Si IV, and narrow forbidden lines. Optical spectra of Sy2 galaxies exhibit instead, both permitted and forbidden narrow lines, because the line of sight points in the direction of the torus, which obscures the BLR.

Low Ionisation Nuclear Emitting Region (LINERs) are also considered as non-jetted AGN. LINERs, with an inefficient accretion rate, show intense forbidden emission lines characterised by a narrower profile and a lower degree of ionisation than that of the Seyfert galaxies. It is not yet clear whether they are indeed a real class of AGN or AGN with inefficient accretion.

The orientation is a significant factor also among the jetted AGN. Jetted AGN viewed at high inclinations are called radio galaxies. They are identified with giant galaxies and quasars. The most important features of radio galaxies are the massive radio jets and lobes that can reach up to several Mpc, well outside the host galaxy. In some cases, radio galaxies show typical AGN optical spectra and they are classified as Broad-Line Radio Galaxies (BLRG) and Narrow-Line Radio Galaxies (NLRG), analogous to Sy1s and Sy2s, respectively. Radio galaxies are classified also based on the properties of the jets as Fanaroff-Riley I (FR I) and II (FR II). FR I sources are fainter and most of the radio emission comes from the surrounding of the nucleus, whereas FR II types are brighter and the radio emission is dominated by the radio lobes far away from the nucleus (Fanaroff and Riley, 1974). FR I sources lie in denser environments and present low accretion efficiency conversely to the FR II sources, which stay in less dense ambiences, characterised by high accretion efficiency.
When the line of sight falls into the relativistic jet, jetted AGN are called blazars. They show continuum variability at all the wavelengths, over short time scales (minutes). Blazars can be divided into Flat-spectrum radio quasar (FSRQ), which optical spectra present emission lines with an equivalent width (EW) larger than 5 Å, and in BL Lacertae Objects (BL Lac), which optical spectra present emission lines with an equivalent width (EW) lower than 5 Å and they are dominated by synchrotron continuum.
According to this view, all objects that possess a quasi-stellar radio core can emit relativistic jets that point in our direction as in the case of blazars, or at wider angles, as in the case of radio galaxies. The two classes FR I and FR II symbolised a difference in luminosity classes but nowadays these sources are classified based on accretion efficiency. High-excitation radio galaxies (FR_{HERG}) present efficient accretion while low-excitation radio galaxies ((FR_{LERG})) exhibit inefficient accretion (Best and Heckman, 2012, Giommi et al., 2012). In 1995, Claudia Urry and Paolo Padovani completed the model by studying the evolutionary scenario and gave an explanation to the FR I population being so close to the BL Lac population and the FSRQs being a subclass of the FR II sources (Urry and Padovani, 1995). The solution involves FSRQs evolving in BL Lac, showing in this way, weaker lines and stronger continuum (Vagnetti, Giallongo, and Cavaliere, 1991). It is clear how the current model is the result of decades of theories, supported by experimental evidence, and successive denials and reformulations in order to catalogue these particular sources. Today there are still many unresolved points. One of these are the narrow-line Seyfert 1 galaxies (NLS1s).

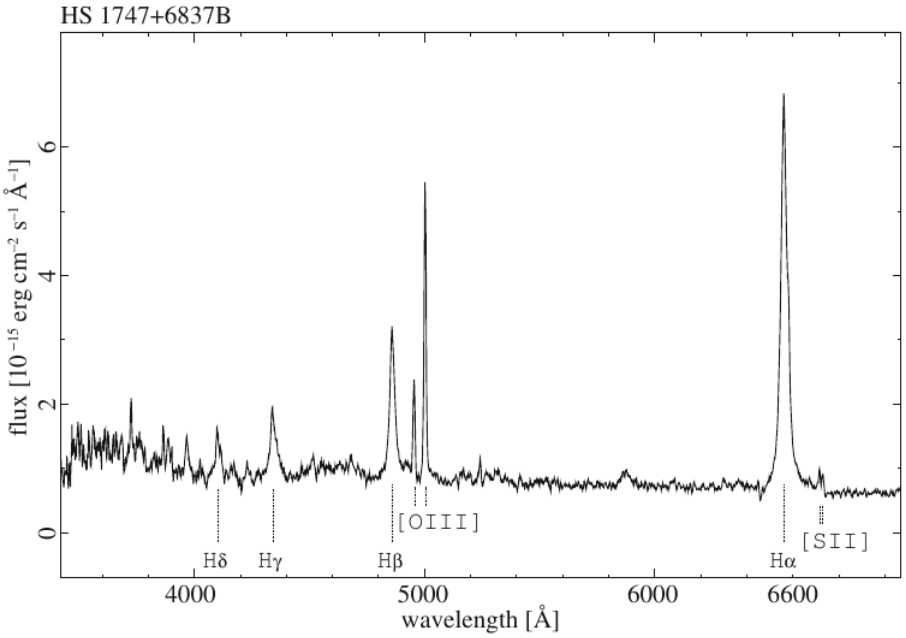

Figure 4: Optical spectrum of the narrow-line Seyfert 1 galaxy HS 1747C6837B (Beckmann and Shrader, 2012).

1.4 NLS1 GALAXIES

First described by Donald E. Osterbrock and Richard W. Pogge in 1985 (Osterbrock and Pogge, 1985), NLS1 galaxies are a peculiar subclass of AGN. A typical spectrum of an NLS1 galaxy is shown in Figure 4.

They are characterised by narrow permitted lines, conversely to Sy1s and slightly wider than those of Sy2s, and by slightly larger forbidden lines (Pogge, 2011). The differences between the spectra of these sources appear in Figure 5. They are identified by an $FWHM(\mathrm{H}\beta) < 2000$ km s^{-1} (Goodrich, 1989) and an [O III]λ5007/H$\beta < 3$ (Osterbrock and Pogge, 1985). Many NLS1s exhibit strong emission of Fe II multiplets. These properties, representative of the spectral classification criteria of NLS1s, are expressed in the anticorrelation between the strong emission of Fe II and the relatively weak emission of [O III]λ5007, placing NLS1s at one end of the main eigenvector of the spectroscopic properties of AGN (Boroson and Green, 1992).

From a physical point of view, the broadening of the lines is due to the gravitational attraction of the BH and the related Doppler effect generated by the motion of the gas around it. The presence of narrow lines in the NLS1 therefore, indicates a low gas rotational velocity around a small-mass BH ($10^6\ M_\odot < M_{BH} < 10^8\ M_\odot$) (Peterson, 2011). Considering also that the bolometric luminosity L_{bol} of these galaxies ($10^{10}\ L_\odot < L_{bol} < 10^{12}\ L_\odot$) is comparable to that of Sy1, it is inferred that NLS1s exhibit a very high accretion rate, close to the Eddington limit (Boroson and Green, 1992). Some NLS1s, in ad-

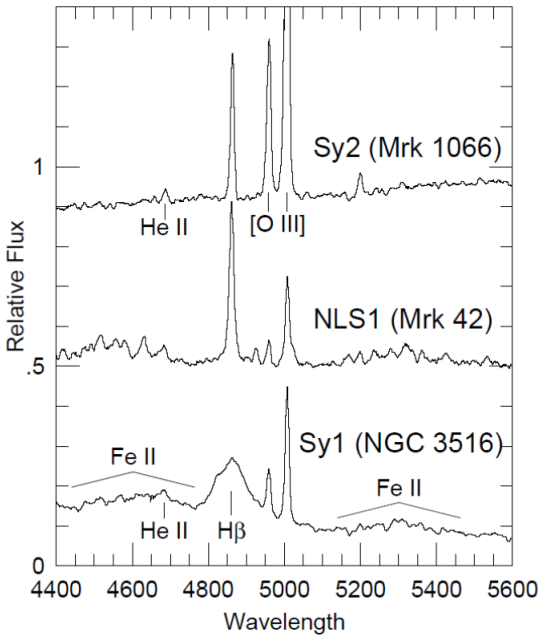

Figure 5: Spectra of the H_β region of three sources: NLS1 Mrk 42, Sy1 NGC 3516 and Sy Mrk 1066 (Pogge, 2011).

dition, even record values higher than this, explained by the fact that the accretion develops with a disk-like geometry while the Eddington relation is based on a spherical symmetry.

According to some authors, these properties would place the NLS1 galaxies in the first phase of the evolutionary scenario of an AGN. They would represent young galaxies and this would explain the small BH mass and the high luminosity (Mathur, 2000a). Some authors, instead, proposed that the low BH mass of NLS1s is due to an inclination effect, caused by the lack of Doppler broadening due to the pole-on view of a disk-like BLR (Decarli et al., 2008).
Because they are classified as Seyfert galaxies, one would expect that NLS1s have no relativistic jets and are therefore classified as galaxies. Recent research has actually found that 7% of NLS1s are brilliant in radio (Komossa et al., 2006), conversely to what had always been claimed. RL galaxies are in fact objects that usually exhibit broad lines from the Balmer series and weak Fe II emission, a property opposite to the These are opposite to those that characterise the NLS1. In the optical spectrum instead, in addition to the above-mentioned characteristics, there is an excess compared to the flux relative to the power-law of the underlying continuum called BBB or Big Blue Bump (Richstone and Schmidt, 1980). It is related to the emission of the accretion disk. NLS1s also exhibit bright emission in the infrared (IR), possibly due to strong star formation and large amounts of dust (Sani et al., 2010, Cracco et al., 2016). Moving to higher frequencies, another important feature concerns the luminosity in X-rays. NLS1s

show steeper spectra than Sy1s in the 'soft' ($0.1 - 2.4keV$) X-rays and that are subject to very rapid variations (scale times $\approx$ 1000s, photon index $\Gamma = -2.5$) ((Boller, 2000)), while some sources exhibit an excess in the ultra-soft ray domain ($E < 1keV$). The shape of the spectrum in the X regions and its relative brightness are also indicators of a high rate of accretion.

1.4.1 *J0354-1340*

The target of this study is the RQ NLS1 6dF J0354328-134008, J0354-1340, (R.A. 03h 54 min 32.85s, Dec. -13d 40m 07.29s, z=0.076).
The radio source J0354-1340 is part of the sample of the southern NLS1s observed by Chen et al. (2020). The observations were carried out with the Karl G. Jansky Very Large Array (JVLA) C-configuration at 5.5GHz. The authors found that this target has a very compact central core at kpc-scale with a flux density of $S_{int} \approx 5.09mJy$. The luminosity and black hole mass measured are $\log(L_{int}) \approx 39.58$ and $\log(M_{BH}/M_{\odot}) \approx 6.99$ respectively. The in-band spectral slope is flat with $\alpha_{in-band} \approx 0.12$. The radio map shows a southern component, that has a separation of $62.2arcsec$ from the central target and with the projected linear size of 93.5kpc. The flux density and luminosity are $S_{int} \approx 1.35mJy$ and $\log L_{int} \approx 39.05$ respectively, which are weaker than the central core. The spectral index of the southern component is $\alpha_{in-band} \approx 1.7$ which is steeper than the core.
The northern component has instead a separation of $55.7arcsec$ from the central target, corresponding to a projected linear size of 83.9kpc. The flux density and luminosity are $S_{int} \approx 0.45mJy$ and $\log(L_{int}) \approx 38.43$ respectively, which are fainter than the southern one. Chen et al. (2020) did not measure its spectral index because it is not detected in the 5 and 6 GHz images.
The optical observations of J0354-1340 were carried out during one night, December 12, 2020, with the Magellan Baade 6.5m telescope at Las Campanas Observatory, Chile, by Dr Enrico Congiu. These observations were performed using the IMACS Short-Camera. During the observation night, the sky was clear, with seeing varying between 0.7" and 1.5". The optical spectrum retrieved is shown in Figure 6. The reduction and the analysis of this optical spectrum were not performed in this thesis.

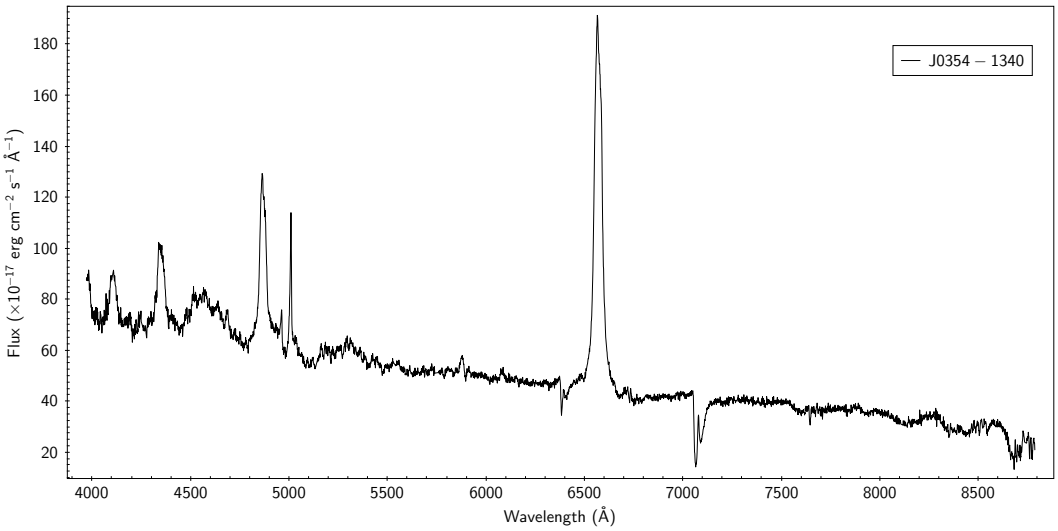

Figure 6: Optical spectrum of J0354-1340.

Part II

RADIO ANALYSIS

2

RADIO ASTRONOMY

Radio astronomy studies radio emission from celestial sources. The range of radio frequencies, ν, or wavelengths, λ, is defined by the atmospheric opacity level. The boundary between radio and far-infrared (FIR) astronomy is placed at a frequency of $\nu \approx 1\text{THz}$ ($1\text{THz} = 10^{12}$ Hz), or at a wavelength of $\lambda = \nu/c \approx 0.3\text{mm}$ (Condon and Ransom, 2016). This also represents the higher boundary of the radio window, while the lower boundary, as shown in the following, does not exist. The atmospheric windows, that is the regions of the electromagnetic spectrum in which the atmosphere is nearly transparent, make ground-based astronomy possible. As shown in Figure 7, only optical/near-infrared (NIR) and radio observations can be made from the ground because the Earth's atmosphere is opaque at most IR, ultraviolet, X-ray, and γ-ray wavelengths. The optical window covers the range of peak thermal emission from $T \approx 3000\text{K}$ to $T \approx 10000\text{K}$ blackbodies and includes the optical emission from hot thermal sources such as stars and star clusters, galaxies and galaxy clusters, hot gas and reflected starlight by cooler objects like planets and moons. The radio window is wider than the visible one and it includes various kinds of astronomical sources and emission mechanisms. The high-frequency boundary of the radio window ($\nu \approx 1\text{THz}$) is given by the vibrational transitions of atmospheric molecules (like CO_2, O_2, H_2O) that absorb most of the radiation from radio sources. Ground-based astronomy is also increasingly degraded at long wavelengths ($\lambda > 1\text{m}$) by variable ionospheric refraction and radio waves having wavelengths $\lambda > 30\text{m}$ are usually reflected back by the ionosphere. Radio emission instead does not have a real lower boundary, so longer radio wavelengths can be observed from space. Furthermore, the radio emission is attenuated by the $T \approx 300\text{K}$ atmosphere. The atmosphere itself also emits radio noise degrading the sensitivity of the ground-based radio observations (Condon and Ransom, 2016).

Since the radio window was been opened, radio astronomy has been considered as the science of serendipity. In the early 1930s, the first astronomical radio source was indeed discovered by chance by Karl G. Jansky. Investigating the interference between the static and the short wave transatlantic voice transmissions, he found a repeating signal of unknown origin, later attributed to the synchrotron radiation produced by Sagittarius A. His pioneering efforts have inspired astronomers in further works. Thanks to radio observations, new unexpected sources were discovered and some optical sources

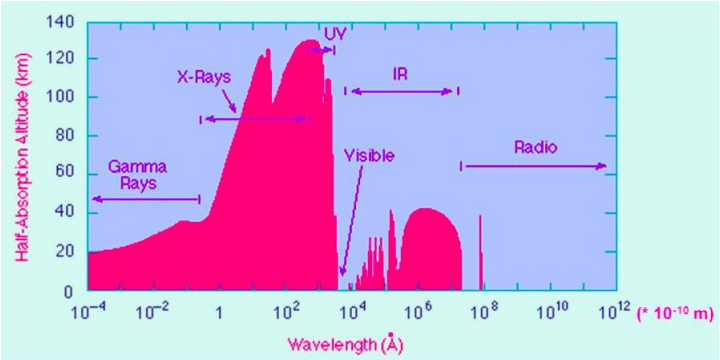

Figure 7: Atmospheric windows of the electromagnetic spectrum. Ground-based astronomy concerns only visible and radio range of the spectrum. Credits: Essential radio astronomy course.

were recognised as peculiar radio objects. Radio astronomy has revealed sources emitting both thermal and non-thermal radiation, and a hidden part of the Universe filled with radio galaxies and quasars powered by supermassive black holes never investigated before. In this way, it has been possible to study in-depth cosmic microwave background radiation from the Big Bang and radio bright objects like pulsars (Condon and Ransom, 2016).
The broadness of the radio window, stretching for five decades of frequencies and wavelengths, opens a wide scenario for investigation. For this reason, radio astronomy requires the use of multiple types of telescopes, different in design, size and configuration, and various techniques of observation. Radio telescopes need very large collectors to observe faint astronomical radio sources. In addition to this, large-diameter (D) radio antennas are required for good angular resolution $\theta_{rad} \approx \lambda/D$, in proportion to the long wavelength, λ, of the electromagnetic radiation being observed. Diameter is also responsible for sensitivity, a measure of the minimum signal that a telescope can distinguish above the random background noise (*Resolution and sensitivity*), and for the field of view (FoV) (*Introduction to Imaging in CASA*).
For this purpose, single dish antennas have been constructed, from smaller telescopes like Metsähovi Radio Observatory (D= 14m), the Sardinia Radio Telescope (SRT, D=64m) or the Green Bank Telescope (D=100m) to the biggest one: the Five hundred meter Aperture Spherical Telescope (FAST, D=500m). Figure 8 shows some of the most important radio telescopes.

2.1 RADIO INTERFEROMETRY

Despite the big diameter of the telescopes, it is still difficult to achieve high resolution with single-dish radio telescopes.

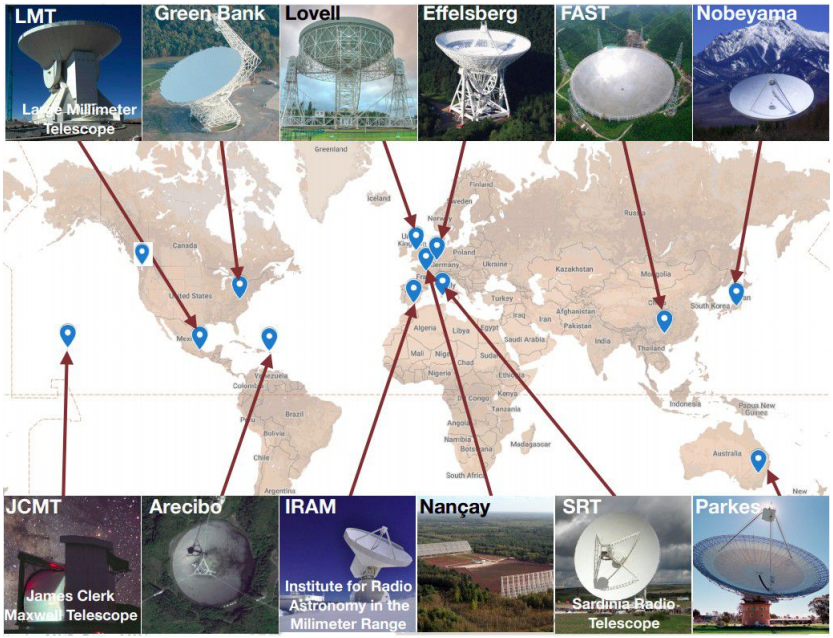

Figure 8: A map of some radio telescopes all over the world. Credits: *Single Dish Astronomy*

For example, the angular resolution at 1.4GHz (21cm) of Green Bank Telescope (D = 100m) is:

$$\theta_{arcsec} \approx (1.2 \cdot \lambda/D) \cdot 2062625 \approx (2.5 \cdot 10^{-3} rad) \cdot 206265 \approx 520'' \quad (7)$$

In order to obtain a resolution of 1″ at 21cm, the radio telescope would need an aperture of ≈ 52km , while the upper limit for a fully steerable radio telescope is D ≈ 100m. The most notable development in solving this problem is the application of the interferometry technique to radio astronomy.
Interferometry is a technique based on the superposition of electromagnetic waves to study the result of their combination, the interference pattern. In the early 1800s, Thomas Young first performed the interference experiment observing the interference image produced by the radiation going through a double-slit.

As shown in Figure 9, the monochromatic planar wave, produced by a coherent light source at wavelength λ, goes through a double-slit screen and for the Huygens-Fresnel principle, the double slits themselves act as a coherent point-like source with the same initial phase. Defining d as the distance between the two apertures, let us consider two parallel rays coming from the slits with an angle θ_a with respect to the perpendicular to the screen. On the optical screen these two signals differ from each other for a phase ϕ:

$$\phi = \frac{2\pi d}{\lambda} \sin(\theta_a) \quad (8)$$

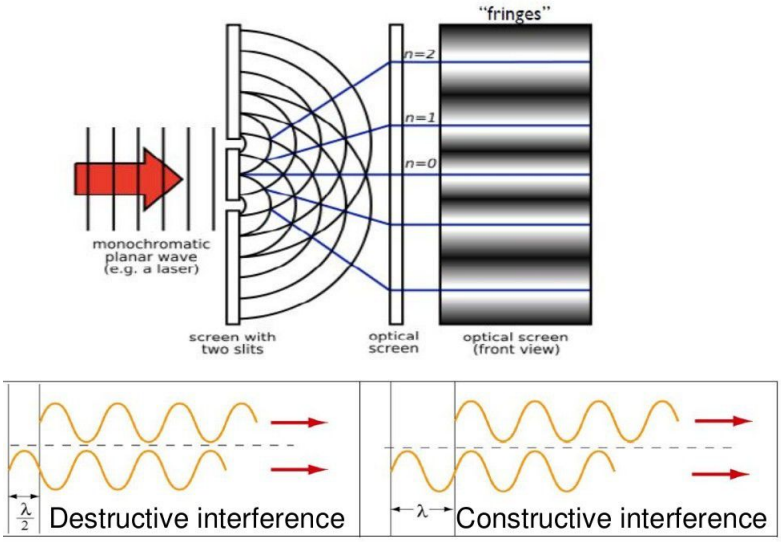

Figure 9: Young's double-slit interferometer. Credits: *Introduction to radio interferometry*

The luminosity distribution observed $I(\theta_a)$, given by the superposition of all the rays produced by the slits, can be expressed as:

$$I(\theta) = I_0[1 + \cos\phi(\theta_a)] \tag{9}$$

where I_0 is the peak intensity corresponding to the image centre ($\theta_a = 0$). The interference image (Figure 9) shows extremely bright regions, corresponding to the maximums of the luminosity distribution, and dark regions, corresponding to the minimums of the luminosity distribution. The succession of these regions is called interference fringes. Constructive interference is possible when the waves are in phase, i.e. when $\phi = 2\pi N$ with N integer number, while when waves are out of phase, destructive interference occurs for $\phi = \pi(N + 1/2)$. The path difference Δ, the difference in the distance travelled by each beam, creates a phase difference between the rays and, taking into account the phase definition (equation 8) it can be defined as:

- For constructive interference: $\Delta = N\lambda$
- For destructive interference: $\Delta = \frac{2N+1}{2}\lambda$

Different types of interference are represented in Figure 9.
Radio interferometry applies the basics of the interferometry technique to radio observations. By building arrays composed of multiple radio telescopes that work together like a single bigger collector, it is possible to achieve higher resolution. Each radio telescope acts as a slit so that the measured interference pattern is produced by multiplying the wave signal received by the different apertures (*Introduction to*

radio interferometry). In cases of extended structures with varying intensity, the phases of the wave signal contain the position information, while the intensity information is in the amplitude. Sources emitting radio wavelengths do not require hard-to-build large-diameter dishes to be observed with high resolution since the angular resolution is a function of the maximum distances between the antennas within the array, called baselines (b), that could be increased as necessary. This technique is called 'Aperture synthesis' or 'imaging synthesis'.
The signal received by each antenna is a linear combination of the radiation coming from the source, the background radiation, the Earth thermal noise and the instrumental noise. The signals arrive at each antenna at slightly different times, depending on the antenna's location in the array (*Introduction to Radio Interferometry*). The signal from each component of the interferometry system is combined with that from every other collector in the correlator, so the interference pattern is due to the combination of the signal observed by pairs of apertures. The central diffraction pattern is defined as the primary beam, i.e., the Fourier transform of the aperture (*Primary Antenna Elements*).
In agreement with the Fourier theory, the signal can be expressed as a sum of sinusoids and the Fourier transform is the mathematical tool that decomposes a signal into its sinusoidal components containing all of the information of the original signal (*Introduction to radio interferometry*). The interference pattern is expressed by the complex visibility function V(u,v), which is the 2D Fourier transform of the source brightness distribution in the sky plane (*Introduction to Imaging in CASA*). The fringe visibility V, or visibility function, can be defined as the ratio between the fringe amplitude and the fringe-average intensity:

$$|V| = \frac{I_{max} - I_{min}}{I_{max} + I_{min}} \tag{10}$$

and it can be also expressed through the Fourier transform as:

$$V(u,v) = \iint T(x,y) e^{2\pi i(ux+vy)}\, dx\, dy \tag{11}$$

where T(x,y) is the brightness of the sky.
Every single observation in which amplitude and phase of the visibility function V(u,v) are measured, is identified by a point of coordinates (u_0, v_0) in the u,v-plane (Figure 10) that is the Fourier Transform plane of the angular distribution of the source in the sky. This plane is defined by two axes (u,v), corresponding to the spatial frequencies of the Fourier transform. Each point in the u,v-plane represents the projected separation between any two telescopes as seen

from the radio source, which are the baselines. An interferometer is sensitive to a range of angular sizes θ:

$$\frac{\lambda}{b_{max}} < \theta < \frac{\lambda}{b_{min}} \tag{12}$$

where b_{max} and b_{min} are the maximum and the minimum baselines. Small structures can be resolved only when their size is bigger than λ/b_{max} but it is always possible to get their flux. Big structures, instead, are resolved only when their size is lower than λ/b_{min}, beyond this boundary they become resolved out and their flux is completely lost. It is possible to observe small structures with the longest baselines having a higher spatial resolution, while big structures can be observed with shorter baselines.
If the angular size of the source is larger than the distance between adjacent positive and negative fringes, produced respectively by constructive and destructive interference, the interferometer's response to it averages to zero, causing the fringe cancellation within the interference pattern. Each baseline detects only a particular spatial scale so the array cannot sample the entire Fourier domain and also the integration time is never long enough to sufficiently cover the uv-plane, so the image is not necessarily complete (*Introduction to radio interferometry*). The orientation of the baseline also determines orientation in the u,v-plane.

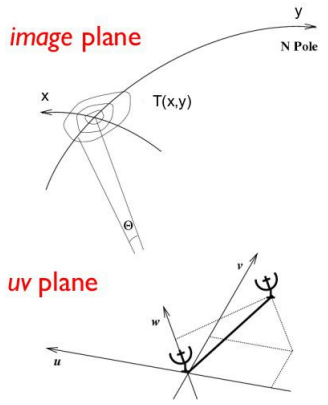

Figure 10: Coordinate system: the source in the image plane and the baseline in the u,v-plane. Credits: *Introduction to Imaging in CASA*

An interferometry system consists of a definite number N of antennas that give $M = N(N+1)/2$ independent baselines leading to a discretization of the visibility function in the u,v-plane. The sensitivity of the system is given by the effective collecting area defined as $\approx N \cdot A_{dish}$, where $A_{dish}(\nu, \tau, \omega)$ is the collecting area of a single telescope and τ and ω are direction coordinates on the sky (*Primary Antenna Elements*). Starting from the coverage of the u,v-plane it is pos-

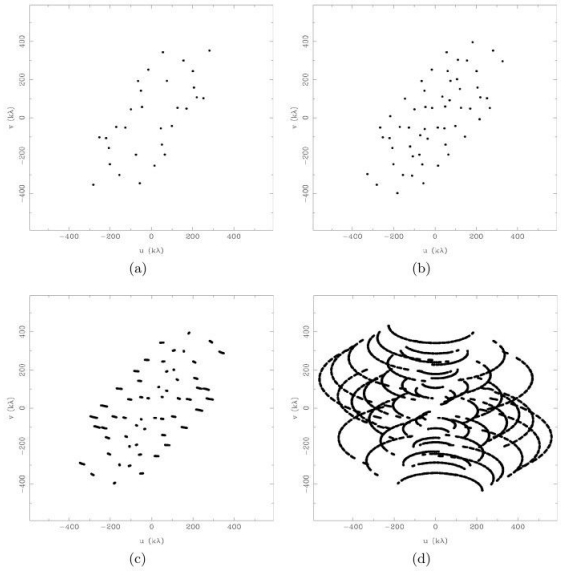

Figure 11: u,v-plane coverage in four different cases: a) 6 antennas with a single observation ($t_{exp} \approx$ 10sec); b) 8 antennas with a single observation; c) 8 antennas with 30 observations ($t_{exp} \approx 5'$); d) 8 antennas with 420 observations ($t_{exp} \approx$ 1h). Credits: Carniani, 2012

sible to reconstruct the intensity distribution of the observed source. A good image quality requires good coverage on the u,v-plane. The Earth rotation aperture synthesis technique uses our planet's rotation to let the projected baselines rotate in the sky plane so at a different time it is possible to measure the visibility function in a different point of the u,v-plane. Increasing the number of antennas and observing the source for a longer time interval are ways to improve the u,v coverage, as shown in Figure 11. In the end, the addition of other telescopes to the arrays with different baselines helps in getting a better u,v coverage.

With a good u,v-plane coverage, the inverse Fourier Transform of the visibility function gives the dirty image. The dirty image, I^D, is the true sky brightness, convolved with the dirty beam D, analogous to the point-spread function in an optical telescope.
The source image in the sky plane is obtained through the deconvolution process, called the cleaning process. This process does not take into account the different responses of each antenna to the acquired signal. The final map is obtained at the end of these procedures. In the next chapter, I will explain how these processes work as tasks of the *Common Astronomy Software Application* (CASA), used to reduce radio interferometric data (*CASA*).
With the application of the interferometry technique to radio observations, in 1946 Martin Ryle and Derek Vonberg first constructed a radio interferometer to investigate cosmic radio emission which had been

discovered by earlier investigators. Over the years, more and larger astronomical radio interferometers have been constructed (Thompson, Moran, and Swenson, 2017). Today, some notable examples are the Atacama Large Millimeter/submillimeter Array (ALMA), composed of 66 antennas situated in northern Chile; the Australia Telescope Compact Array (ATCA), made of six identical 22m diameter dishes placed in Australia; the Giant Metrewave Radio Telescope (GMRT) Observatory, located near Pune in India, that is an array of thirty fully steerable parabolic radio telescopes of 45-metre diameter. Very-long-baseline interferometry (VLBI) is instead a type of astronomical interferometry in which the incoming radio signal is collected by multiple radio telescopes that do not need to be members of the same array, so the distance between them increases. The telescopes part of this interferometer can be placed in different countries or even in space. The Very Long Baseline Array (VLBA) is a VLBI array, placed across the United States and it consists of 10 telescopes of 25m diameter. The European VLBI Network (EVN) is a network of radio telescopes located primarily in Europe and Asia, with additional antennas in South Africa and Puerto Rico (Arecibo, 305m), composed of 21 telescopes. VLBA and EVN can be connected to form a global VLBI network, in which resolution of milliarcsec is the maximum resolution achieved with radio interferometry.

2.2 JVLA

The observations of the object of this study, J0354-1340, were carried out with the JVLA C-configuration at 5.5GHz (Figure 12). The JVLA belongs to the National Radio Astronomy Observatory (NRAO) built throughout the 1970s, and it is a centimetre-wavelength radio astronomy observatory located in central New Mexico on The Plains of San Agustin. Such location was chosen to prevent human radio interferences, as The Plains are a stretch of desert ringed by mountains and far from any city. The desert climate, in addition, is crucial for radio telescopes collecting radio waves at the same frequencies of water transition radio waves to reduce the background signal from Earth-based water molecules (*Very Large Array*). The JVLA is formed of 28 parabolic dish telescopes (27 actives and one that is a spare), and each antenna has a dish diameter of 25 metres. The wider an array is, the more resolution it is possible to achieve. The JVLA presents four different configurations, designated A (the most elongated, the longest baselines of 36.1km, resolution on the smallest spatial scale: 8.9″ at 6GHz) through D (the tightest, the shortest baselines of 1.03km, resolution on the largest spatial scale: 240″ at 6GHz). The C configuration, used for this study, has a length of 3.4km and a resolution on the large spatial scale of 3.5″ at 6GHz.
The iconic "Y" shape of the JVLA (Figure 13) is functional to have

Figure 12: The Karl G. Jansky Very Large Array. Credits: https://xevio.us/2015/02/vla/

three long arms of nine telescopes each and to allow the flexibility of stretching the arms when the configuration changes, with the aim of change resolution, the field of view, and sensitivity. The system usually cycles through all the various possible configurations (including some hybrids) every 16 months and the frequency coverage is 74MHz to 50GHz. In 2011, the VLA expanded its technical capacity through an upgrade project replacing the original electronics with state-of-the-art equipment. For these reasons, a new name was proposed for the array, and in 2012 it was renamed as the "Karl G. Jansky Very Large Array". Finally, the JVLA has evolved into the Expanded Very Large Array, enhancing the instrument's sensitivity.

In the next chapter, I will describe in detail the software used for data reduction and the procedure applied.

Figure 13: The "Y" shape of the JVLA seen from above. Credits: *The National Science Foundation's Jansky Very Large Array*.

3

DATA REDUCTION

This Chapter is dedicated to the description of the data reduction procedures applied in order to obtain the radio map, the spectral index map, and the tapered map of the NLS1 J0354-1340, the target of this work.

3.1 DATA DESCRIPTION

The radio source J0354-1340 is part of the sample of the southern NLS1s observed in the JVLA project (Proposal ID: VLA/18B-126, PI S. Chen). The observations were carried out to study the radio morphology of NLS1s in the southern hemisphere (Chen et al., 2020), increasing the former sample of known radio-detected NLS1s. This study proved that most NLS1s are unresolved at kpc-scale and that in general radio emission is concentrated in the central region. Chen et al. (2020) stated that the radio emission of steep NLS1s is dominated by misaligned jets, AGN-driven outflows, or star formation superposing on a compact core while in the case of flat NLS1s the radio emission may be produced by a central core that has not yet developed radio jets and outflows. The authors confirmed also that only a few sources show diffuse emission and discovered new NLS1s harbouring kpc-scale radio jets, including J0354-1340.
The observation of J0354-1340 was carried out in February 2019 with the JVLA in C-configuration, centred at 5.5GHz with a bandwidth of 2GHz. The exposure time was 30 minutes and the angular resolution 3.5 arcsec, yielding a theoretical image sensitivity of $\approx 7 \mu Jy beam^{-1}$. This setting allowed to obtain data with resolution and sensitivity high enough to discover extended structures. The measurement set is composed by 16 spectral windows (centred at 4.55, 4.68, 4.81, 4.94, 5.06, 5.19, 5.32, 5.45, 5.55, 5.68, 5.81, 5.94, 6.06, 6.19, 6.32, 6.45 GHz), (Chen et al., 2020). The data are also averaged in time (10 sec) and frequency (64 channels). I reduced the data using the CASA version 5.6.2-3.

3.2 CASA

I reduced the data using the JVLA calibration pipeline version 5.6.2-3 and the CASA version 6.1.2-7, which supports IPython 5.1.0. CASA is a data processing software used for radio data, developed by an international consortium of scientists under the guidance of NRAO.

This software can process data from both single-dish and aperture-synthesis telescopes and it is able to support the data reduction and imaging pipelines for ALMA and JVLA (CASA documentation). The functionality within CASA has been divided into tasks and tools: the CASA tasks are Python scripts using the CASA tools, that are commonly performed when analysing astronomical data. CASA uses its own internal data structure, called a Measurement Set (.ms), which is a set of tables containing the data from the observations. Users are allowed to import ALMA and JVLA data through import facilities.
Data processing in CASA (Jaeger, 2008) develops through:

- *Data flagging*: it is possible to remove bad data manually through a task, or interactively with either the plotter and/or viewer graphical user interfaces (GUIs).

- *Calibration*: it is the application of correction factors to make the measured quantities similar to the ideal ones for interferometric data. Sometimes other processes are applied before calibration like temperature correction, atmospheric corrections, and modelling flux density. The process can be divided into some discrete phases: calibrator model visibility specification, setting model visibilities for calibrators; prior calibration, setting up previously known calibration quantities that need to be pre-applied, e.g. antenna position offsets or atmospheric models; bandpass calibration, solving for the relative gain of the system over the frequency channels in the dataset (if needed); gain calibration, solving for the gain variations of the system as a function of time; polarisation calibration, solving for polarisation leakage terms and linear polarisation position angle; establish flux density scale, if only some of the calibrators have known flux densities, then derive flux densities of secondary calibrators; if necessary smooth calibration (*Synthesis Calibration*). A designated calibrator source is used for these steps, a bright quasar near the target is usually observed for gain and bandpass calibration or also a solar system object for absolute flux calibration.

- *Imaging*: it is the use of the facilities for creating and manipulating images from calibrated data (measurement sets). The image creation consists of stages of Fourier transforming observed interferometric data (visibilities) and image based deconvolution. CASA includes a variety of weighting schemes (natural, uniform and briggs) to be applied to the visibilities. Natural weighting gives each sample of visibilities the same weight and since there are many samples at short baselines, it gives the largest beam and the best surface brightness sensitivity. Uniform weighting gives each visibility a weight inversely proportional to the sample density and it weighs down short baselines

so that long baselines are more pronounced. Uniform weighting provides the best resolution. Briggs weighting is a graduated scheme using the robust parameter and represents a compromise of noise and resolution. Robust value ranges from -2 ($\approx$ uniform) to +2 ($\approx$ natural). Taper is an additional weight function to be applied, typically a Gaussian to suppress the weights of the outer visibilities. The resulting dirty images are then deconvolved. CASA supports different versions of the deconvolution algorithms available like CLEAN, Maximum entropy methods (MEM) and Non-negative Least Square (NNLS) based deconvolution. It is possible to use both non-interactive and interactive clean modes. The clean algorithms supported by CASA are Hogbom CLEAN (classic cleaning algorithm), Clark CLEAN (minor/major cycles), Cotton-Schwab CLEAN (Clark algorithm, with altered major cycle), and Multi-scale CLEAN (delta-functions and circular Gaussians). These algorithms can be applied to a single field or mosaic fields or even wide fields.

Other CASA facilities and interfaces are:

- *Simulator*: facilities able to simulate observations from the JVLA and ALMA telescopes.
- *User Interface*: usually users interact through the interactive IPython shell but there are also graphical interfaces like plotter (the plotting facilities in CASA uses the Python library and are used to plot calibration data, measurement sets and simple tables), logger (it displays any messages reported by the CASA software), table browser (to investigate the contents of a table) and viewer. The Viewer can be used to view both images (CASA and FITS formats) and visibility data (CASA measurement sets). The CASA viewer can handle a large number of frequency channels, it can play animations and images can be overlaid on top of each other (the contour map onto the raster image, for example).
- *IPython*: the command-line interface. It is possible to import Python libraries into the CASA environment and use them from within CASA.

3.3 MULTISCALE MULTIFREQUENCY SYNTHESIS (MS-MFS)

To produce the radio map, the spectral index map, and the tapered map starting from the measurements set data (file.ms) I used the multi-scale multi-frequency deconvolution method. The ms-mfs algorithm models the wide-band sky-brightness distribution as a linear combination of spatial and spectral basis functions, and performs image-reconstruction (Rau and Cornwell, 2011, CASA Task Reference Manual).

3.3.1 *tclean*

First of all, I applied the CLEANing process to the data through the *tclean* task and then the *self-calibration* to obtain in two steps the radio and the tapered map. The *tclean* task forms images from visibilities and reconstructs a sky model (CASA Task Reference Manual). Taking into account the brightest pixels in the dirty image I^D (that is the convolution between the real signal coming from the source and the dirty beam), the algorithm creates a model as a linear combination of point-like sources based on the position and intensity of the brightest pixels. Then, the model multiplied by the dirty beam is subtracted from the I^D creating the residuals image I^R. This is the deconvolution process. The task searches the brightest pixel in the residual image and repeats the procedure until the number of iterations is bigger than the value set or the maximum value of intensity in I^R is lower than a fixed value. At the end of the process, the real sky brightness image is obtained. The clean regions can also be defined manually, using interactive clean.
The task parameters can be chosen by the user.
Imsize is the size of the region where the map will be created and it is defined by the number of pixels centred on the phase centre defined by the user. In our case, the source coordinates are close enough to the pointing centre that I did not need to modify it. I set *imsize*=4096 so a region of 4096x4096 pixels was investigated to check for the presence of nearby sources. I chose to use a *cell* of 0.2 arcsec to properly sample the beam. The values are shown in Table 1. The *deconvolver* is the minor cycle algorithm, which operates on residual images and produces output model and restored images. This parameter was set on 'multiscale (term) multifrequency synthesis' (mt-mfs). The number of Taylor coefficients in the spectral model, *nterms*, tells how many terms are being fitted to the spectral information and its value was fixed to 2 (the spectrum is a straight line with a slope in log-space). For the maximum number of iterations *niter*, a stopping criterion based on total iteration count, was chosen a value of 20000. The *gain* is the fraction of the source flux to subtract out of the residual image. It represents how much source is cleaned up in a cycle and it is usually set to 0.1 for a point-like source while for an extended source like J0354-1340 the gain was fixed to 0.05. I put the maximum number of minor-cycle iterations (per plane) before triggering a major cycle, *cycleniter* equal to 2000. For *pblimit* value, which gives a threshold below which image values are set to zero, -1.5 was chosen to see a large enough region needed to clean also the nearby sources. Sometimes in the dirty image I^D, artefacts called sidelobes appear because of a non-complete coverage of the uv-plane (*Interferometry basics*). These fake structures are very symmetric but do not represent real emissions. The sidelobes for the JVLA often look like six spokes radiating out from a bright

source. If there is a bright source with sidelobes contaminating the target then it is necessary to expand the mapped region to a larger one containing this bright source in order to model it and reduce its effects. This problem becomes more important in compact array configurations such as C and D, because the beam and the field of view are much larger than in A or B configuration, so many more neighbouring sources are included. Hence, in the case of J0354-1340, the field of view was enlarged. During gridding of the dirty or residual image, each visibility value is multiplied by a weight before it is accumulated on the uv-grid. The weighting parameter was set to *briggs weighting* that provides a compromise between natural and uniform weighting and therefore offers a compromise between spatial resolution and surface brightness sensitivity and also suppresses sidelobes (VLA CASA Imaging Manual). The robust value was fixed to 0.5. In the end, I had to put *Interactive*=True to clean manually the source.
The process ends with the interactive CLEANing through the viewer display panel. For this first stage of cleaning, I selected first only the central brightest pixels to be cleaned, in two steps, because self-calibration need only the emission from the centre. Once the region was selected, *tclean* extracted flux from the residual image convolved with the PSF model and created the source model.
At the end of the clean process, the task produces:

- *Output image*: the true image of the sky source brightness
- *sourcename.psf*: image of the point spread function
- *.residual*: residual image
- *.image*: restored image
- *.model*: model image
- *.sumwt*: single pixel image containing sum-of-weights
- *.pb*: primary beam model
- *.alpha*: spectral index map
- *.alpha.error*: estimate of error on spectral index map

For multi-term wideband imaging, except for the alpha and the alpha.error images, all the other images will have additional .tt0, .tt1 suffixes to indicate Taylor terms. (CASA Task Reference Manual).

3.3.2 *Self-calibration*

Data are affected by errors due to the different antenna responses to the acquired signal, the presence of the atmosphere producing distortions, and instrumental effects. Self-calibration, the calibration of the

source visibilities through a model of the source itself, is an important technique used to reduce noise. It is used both for point sources and extended structures.
A standard calibration is applied by the pipeline before the self-calibration, it usually uses quasars with rather constant flux densities, that are point-like sources. For J0354-1340, Chen et al. (2020) used 3C 147 as the main calibrator and J0405-1308 as the phase calibrator. The aim is to observe sources with known flux, shape and spectrum to derive the response of the instrument. In this way, bandpass calibration compensates for the change of gain with frequency through observations of a strong source with a flat spectrum, i.e. bandpass calibrator. Phase calibration compensates instead for relative temporal variation of the phase of the correlated signal on different antennas (or baselines) through observations of a strong source with a known shape, preferably a point-like one, every few minutes. Amplitude calibration offsets atmospheric opacity and loss of signal within the interferometer thanks to observations of a source with known flux. This can be a planet or a stable radio source (*Interferometry basics*). After the standard calibration is applied, there may be residual phase and/or amplitude errors in the calibrated data of the target source that degrade the image quality. Self-calibration processes are applied to reduce the phase and amplitude errors in the visibilities of the same target source, using a model of the target source itself NRAO (*VLA Self-calibration Tutorial*). The calibration process of the dirty data produces calibration tables to be applied to the source visibilities. The source model, the intensity distribution in the sky plane, has been created in the previous step by the CLEANing process of the calibrated data. The model is thus transformed into visibilities through Fourier Transform and new tables of calibration are created for the source from the source itself. The calibration solutions are directly applied to the target field from which they were derived.
For this purpose, I used the task *gaincal* which is both for general gain calibration using an external calibrator and for self-calibration (CASA Self-Calibration Manual). The calibration mode *calmode* was set to 'p', indicating that self-calibration is performed only on phase because amplitude self-calibration has a larger potential to change the source characteristics (i.e. introduce artefacts). I applied only one cycle of phase-only self-calibration to J0354-1340, choosing the temporal interval of solutions *solint* equal to 180s. The solution interval values range all over the whole integration period and it is important to choose a value to be short enough so that it tracks changes in the atmospheric phase with high accuracy, but long enough so that you measure phases with good signal-to-noise. The value of 180 s is often used as the maximum because in this time range there should not be considerable changes in the atmosphere at radio frequencies. During this stage, the task is still finding flagged solutions that are bad and

will be ignored and it creates the table with calibration solutions.
At this point I used the task *applycal* to apply the calibration, setting the value of *gaintable* to caltable, in order to apply the solutions created with the previous task to the visibilities, and setting the value of *applymode* to calflag. After running the task the original visibility file will be changed. At this point, the CLEANing process was carried out again.
Conversely to the first stage, I had to clean manually not only the central brightest pixels but also the regions with bright emission that became visible gradually during the CLEANing procedure. The image showed very bright sidelobes and a possible fake emission in the north. This artificial structure could be the sidelobe of another source or just noise. Since it was unclear whether the northern emission was real or not, I decided to do two different versions of the map: one in which I cleaned the northern emission cleaned and one in which I did not clean it. However, it is worth noting that the NVSS image of J0354-1340 shows an elongated structure in the north direction. Therefore, it is likely that the emission in the north is real.

3.3.3 *Radio map*

The last step to obtain the final map was to apply the largest cleaning to make sure that all the flux was collected and also reducing sidelobes in this way. In this way, I obtained the first final map (Figure 14). The σ of this image, that is the *root mean square* rms, was 8 μJy. The Relative Contour Levels were -3, 3 $\times 2^n$ $n \in [0, 7]$. In this case, the sidelobes have negative contour levels (dashed lines) and there is no evidence of the potential emission located in the northwest side of the nucleus.
For the second version of the final map, before doing the largest cleaning, I cleaned also the northern emission. The rms is 8 μJy and the Relative Contour Levels were the same as before(Figure 15).

3.3.4 *Tapered maps*

Since J0354-1340 shows extended structures, a taper was used to enhance the extended emission sensitivity. Higher spatial frequencies are weighted down relative to lower spatial frequencies to delete artefacts coming from poor coverage regions of the uv-plane. The taper works by convolving the visibilities with a Gaussian centred on the short baselines. It can be specified either as a Gaussian in uv-space (e.g., units of lambda) or as a Gaussian in the image domain (eg. angular units like arcsec), (CASA Task Reference Manual). Before the last CLEANing process, I fixed the value of *uvtaper* in the task. The uvtaper should be approximately 5-15% of the maximum λ, which is

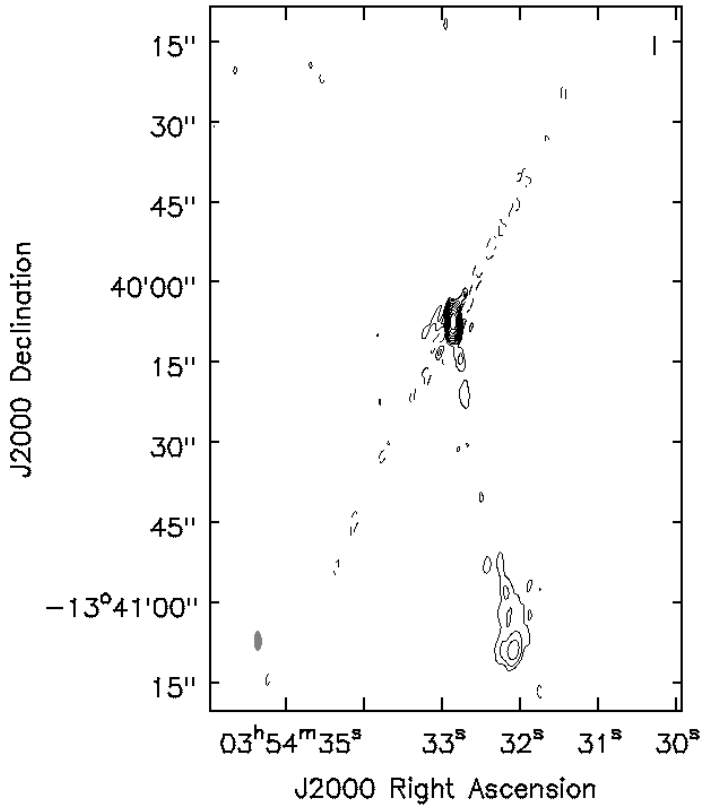

Figure 14: Radio map of J0354-1340 with a σ=8 μ52km.

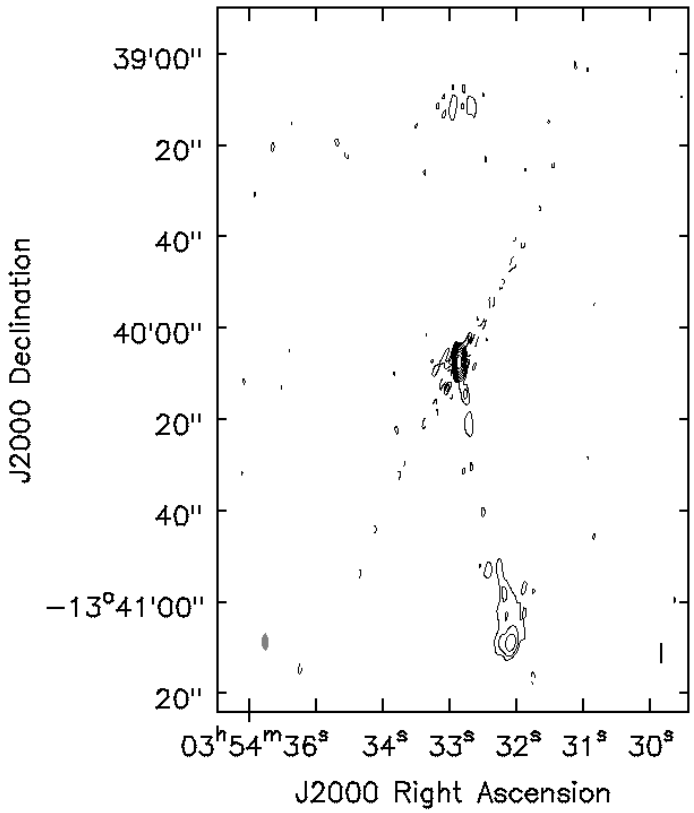

Figure 15: Radio map of J0354-1340 with the northern emission cleaned, σ=8 μJy.

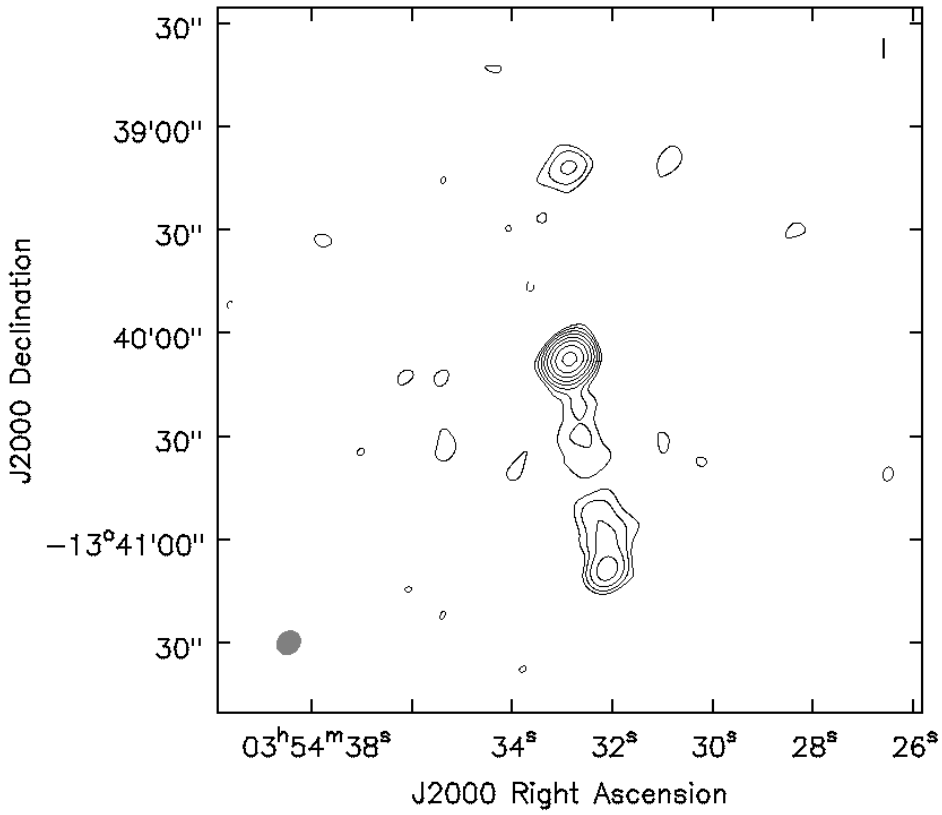

Figure 16: First version the tapered map of J0354-1340 obtained without cleaning the northern emission and with *uvtaper*=15kλ and rms=10 μJy.

the largest number of wavelengths it is possible to fit into a baseline. In this case, this number is ≈ 220 kilo-λ (kλ), so I set the uvtaper value to 15 kλ. I also tried with 10, 20 and 25 kλ values but uvtaper = 15kλ was the best compromise between sensitivity and resolution. During the last CLEANing process, I did the manual cleaning twice with cycleniter=2000.
The first version of the tapered map, in which the northern emission was not clean, was obtained setting the rms=10 μJy (Figure 16).

The second version of the tapered map, with the northern emission cleaned, was instead obtained setting the rms=11 μJy (Figure 17).

3.3.5 *Spectral Index Map*

Starting from the final map, I obtained the spectral index (α_{nu}) map. The primary beam size is a function of the frequency. It is smaller at higher frequencies and larger at lower frequencies. The range of

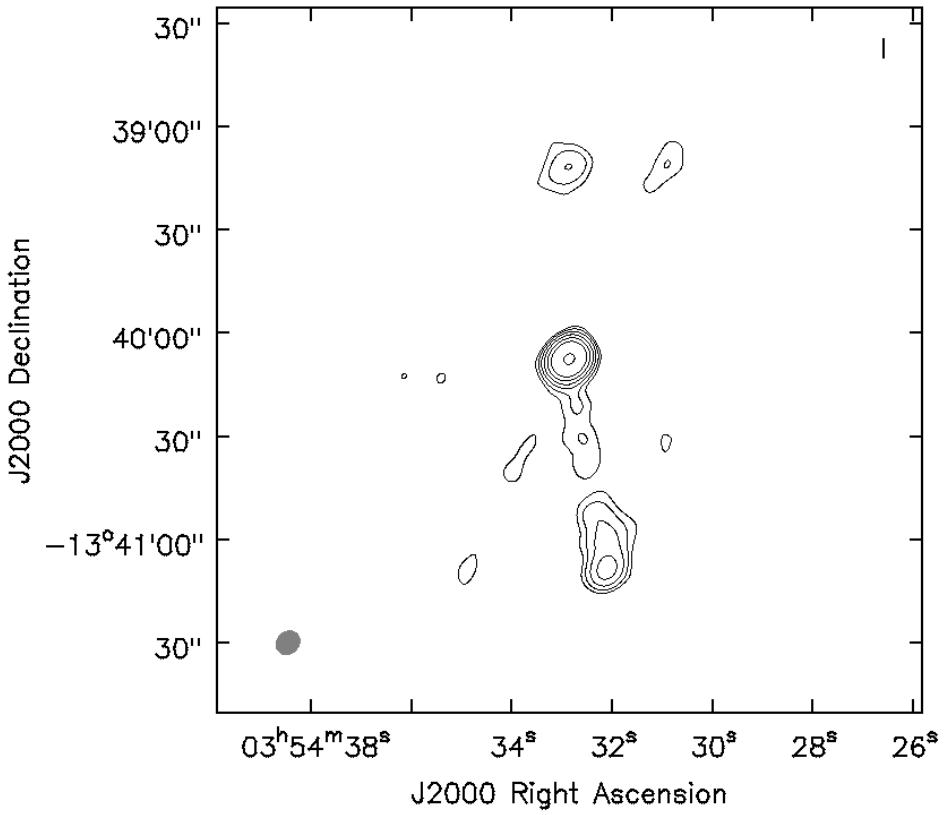

Figure 17: Tapered map of J0354-1340 obtained with *uvtaper*=15kλ and rms=11 μJy.

frequencies at which J0354-1340 was observed goes from 4.5GHz to 6.5GHz so the beam varies with frequency through this range and imposes its own spectral index to the map. To correct for this effect I used the task *widebandpbcorr*: wide-band primary beam correction. Setting the threshold to 5 times the rms, the task removes all the values that are less significant than 5 σ, because the emission below this threshold has a too low S/N to reliably estimate the spectral index. I used 0.4 mJy as a threshold and -1.5 as pbmin. This procedure created a primary beam corrected image.
However, the spectral index map still contains errors. To remove the bad data, CASA offers an opportunity to mask values or pixels with high errors. The mask values were chosen using the threshold in the α_{nu} error map. CASA kept the mask that the image already had and added another mask which is limited to the condition of the error lower than 1, leaving out most of the clearly erroneous values and keeping the α_{nu} values associated with the source.

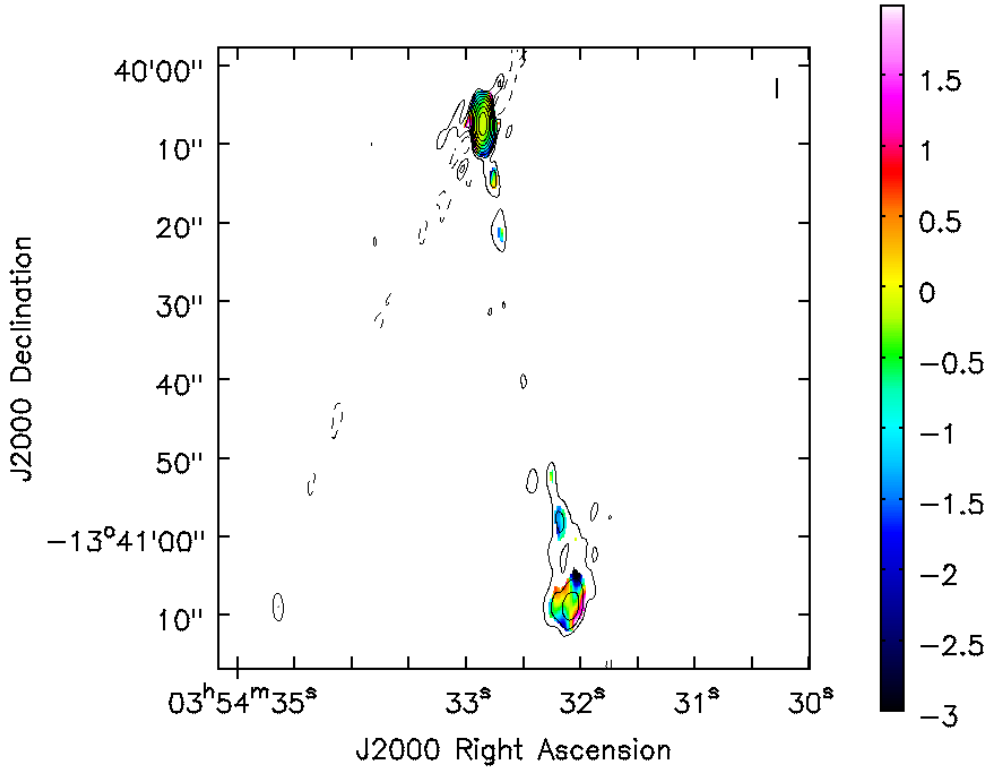

Figure 18: Spectral index map of J0354-134. This map shows only the core and the southern emission.

Once the mask is added, errors have been removed from the spectral index map. The α_{nu} and its associated error are calculated for each pixel but pixels are not independent. For this reason, the beam in the image header was forced to be the size of one pixel and was then convolved with a Gaussian that represents the size of the real clean beam. To achieve this, the area of one pixel was calculated as:

$$Area\_pixel = (cell\_size)^2 = (0.2arcsec)^2 = 0.04arcsec^2 \quad (13)$$

Considering a circular beam, so major axis equals the minor axis, I set its area equal to the one calculated before, in order to find the radius of the artificial beam itself:

$$\pi r^2 = 0.04arcsec^2, \qquad r = \sqrt{\frac{0.04arcsec^2}{\pi}} = 0.1128arcsec \quad (14)$$

MAJOR BEAM	MINOR BEAM	BEAM POSITION ANGLE
3.5320 arcsec	1.2978 arcsec	1.6280 deg

Table 1: Original values of the beam

Since the beam radius r is half of the FWHM, the pixel-sized beam will have:

$$FWHM = 2r = 0.226arcsec \tag{15}$$

Through the task *imhead* I saved the values of beam_major, beam_minor and beam_positionangle written in the CASA logger (Table 1) and then I substituted the first two values with the FWHM just calculated and the latter with zero. In this way, the pixel-sized artificial beam was added to the header of the spectral index map image. The last step was the convolution of the image with a Gaussian of the size of the correct clean beam through the *imsmooth* task. Taking into account the dependency of the pixels and convolving the α_{nu} map and its error map with the clean beam considerably decreases the pixel-to-pixel variations, and also the error.

The spectral index map obtained shows a data range of [-1,1] (Figure 18).

4

DATA ANALYSIS

In this chapter, I will analyse the results obtained through the data reduction processes.

4.1 MEASUREMENTS

J0354-1340 seems to be an FRII radio galaxy (Fanaroff and Riley, 1974), with a compact central core bright at radio frequencies, probably being the jet-base having a flat in-band spectral index (Chen et al., 2020). This source shows extended emission located on the southern-west side and on the northern-east of the source nucleus, corresponding to the very elongated jets, as is possible to observe in Figure 15. The spectral index map (Figure 18) shows a flat core, as typically seen in blazars. The spectral index of the lobe seems to be $\approx$ -0.5 which is slightly higher than the characteristic spectral index of -0.7 of optically thin synchrotron emission. This may be due to interaction between the lobe and the intergalactic medium (IGM), which re-accelerates the electrons in the lobe and thus makes the spectral index flatter.
I measured the peak and the extended emission flux of J0354-1340 from the radio map. I did these measurements for the core and for the extended emission. Through the *viewer*, first of all, I draw a square around the central region and I used the *2D Gaussian fitting tool* that fitted the core region with a 2D gaussian on the radio map. The source was modelled with a Gaussian fit and deconvolved from the beam, to obtain the integrated and peak flux densities centred at 5.5GHz. The measured values and the related errors produced by CASA are reported in Table 2.

Peak flux	5.254 $\pm$	0.020 mJy beam^{-1}
major axis FWHM	3.53	arcsec
minor axis FWHM	1.30	arcsec
position angle	1.63	deg

Table 2: Flux and Image component size (deconvolved from the beam)

The extended emission in the map is not continuous but it shows up in three distinct emission regions, and I measured all of them. I followed the outermost contour that it is the 3 σ contour. The total

flux density has been measured as the sum of the flux density of all the regions considered. The error related to whole extended emission has been estimated as the rms usually used (8 μJy) multiplied by the square root of the area covered by the outermost contour (sum of the number of points Npts) expressed in units of beams (the size of beam given in pixels) (Berton et al., 2018).
In Table 3 are reported the number of points and the flux density, measured for every region and for the total extended emission.

REGION	NUMBER OF POINTS	FLUX DENSITY
Core	1219	4.88 mJy
S1	183	46.0 μJy
S2	2039	0.6974 mJy
S3	81	18.1 μJy
S4	37	7.44 μJy
N1	185	43.4 μJy
N2	174	42.2 μJy
Total	3918	5.73 mJy

Table 3: S refers to the different regions of the southern emission: S1 is the region closer to the core, located in the southeast part; S2 is the biggest region in the southern-east part; S3 is the small region in the northwest part of the biggest region and S4 is the smallest region in the northeast part of the biggest region. N refers to the different regions of the northern emission: N1 is the region located on the east-side of the emission; N2 is the region located on the west-side of the emission. The Beam Area ($Area_{Beam}$) measured for every region is 129.843.

The core, south and north regione error is the rms per beam and was calculated as:

$$(rms/beam)_{core} = rms \cdot \sqrt{\frac{Npts_{tot}}{Area_{Beam}}} = 8\mu Jy \cdot \sqrt{\frac{1219}{129.834}} = 24.51\mu Jy \tag{16}$$

$$(rms/beam)_{north} = rms \cdot \sqrt{\frac{Npts_{tot}}{Area_{Beam}}} = 8\mu Jy \cdot \sqrt{\frac{3918}{129.834}} = 13.30\mu Jy \tag{17}$$

$$(rms/beam)_{south} = rms \cdot \sqrt{\frac{Npts_{tot}}{Area_{Beam}}} = 8\mu Jy \cdot \sqrt{\frac{3918}{129.834}} = 33.70\mu Jy \tag{18}$$

The analysis of the observations of J0354-1340 at 5.5 GHz has given:

- Total flux density of $S_{tot} = 5.73 \pm 0.04$ mJy,
- the peak flux of $S_{peak} = 5.25 \pm 0.02$ mJybeam^{-1}.

I also estimated the deprojected linear size, the orientation and the age of the jet. I did two different estimates of each quantity, considering first that the jet is propagating at the speed of light $c = 3 \times 10^5$ km/s and then taking into account the more realistic $v_{jet} = 0.3c$ (Giroletti and Polatidis, 2009, Berton et al., 2020). To do that, I calculated the ratio between the flux density of the southern emission and the flux density of the northern emission. Starting from the tapered image shown in Figure 17, the one with the northern emission cleaned, I used the task *imfit* to fit a Gaussian on the centre of the source and then extract it from the image to have the residual emission without the core component. The southern emission appears brighter than the northern one, meaning that the southern component is the approaching jet, the one pointing toward our line of sight, while the receding jet is identified with the northern component. The FRII radio galaxy usually shows intrinsically symmetric morphology. In the case of J0354-1340, the jet and the counter jet flux values differ due to the Doppler effect that amplifies the observed flux of the approaching jet (f_+) and diminishes the observed flux of the receding jet (f_-), leading to different Doppler enhancements. Starting from the flux ratio derived from the Doppler factors (Beckmann and Shrader, 2012):

$$\frac{f_+}{f_-} = \left(\frac{1 + \beta \cdot \cos(\theta)}{1 - \beta \cdot \cos(\theta)}\right)^{(2-\alpha)} \tag{19}$$

I derived the inclination of the jet θ, the angle with respect to the line of sight. As shown in the equation 19, the ratio between the flux of the approaching jet (f_+) and the flux of the counter jet (f_-) depends on:

- the cosine of θ;
- $\beta = \frac{v}{c}$, the ratio between the velocity of the jet v and the speed of light c. I approximated this value to 0.99, when it is assumed that the jet is propagating approximately to c, and to 0.3 when I considered the relativistic approximation. In fact, β is lower than one, so the inclination obtained from the first approximation will be the upper limit of θ;

- α, the spectral index of the jet, related to the slope of the electron population energy distribution. In this case, I set $\alpha = -1$.

The flux densities were measured in the *viewer* drawing a region around the southern and northern emissions, giving respectively $f_+ = 0.77 mJy$ and $f_- = 0.09 mJy$. Considering $\beta = 0.99$ I obtained:

$$\frac{0.77e-03}{0.09e-03} = \left(\frac{1+0.99\times\cos(\theta_1)}{1-0.99\times\cos(\theta_1)}\right)^3 = 8.6, \qquad \cos(\theta_1) = \frac{1}{3} \tag{20}$$

The equation 20 gives an estimate of the jet inclination of $\theta_1 = 70°$. This value represents an upper limit for the inclination of the jet since the velocity of the jet is never so close to c.
For this reason, I calculated the inclination with a more realistic value for the jet velocity, choosing $\beta = 0.5$:

$$\frac{0.77e-03}{0.09e-03} = \left(\frac{1+0.5\times\cos(\theta_2)}{1-0.5\times\cos(\theta_2)}\right)^3 = 8.6, \qquad \cos(\theta_2) = \frac{1}{1.5} \tag{21}$$

The equation 21 gives a more reasonable estimate of the jet inclination of $\theta_2 = 47°$.

Finally, taking into the account $\beta = 0.3$:

$$\frac{0.77e-03}{0.09e-03} = \left(\frac{1+0.3\times\cos(\theta_3)}{1-0.3\times\cos(\theta_3)}\right)^3 = 8.6, \qquad \cos(\theta_3) = \frac{1}{0.9} \tag{22}$$

In this case, it is evident that it is impossible to derive a value for the inclination with this flux ratio. The relativistic approximation of $v = 0.3c$ is not valid for the jets of J0354-1340.
To have the deprojected linear size of the jet, first of all, I calculated the distance of the source D, with the NASA/IPAC Extragalactic Database (NED) cosmology calculator (Cosmology Calculator I). To obtain the luminosity distance D_L, I set the redshift to $z = 0.076$, the Hubble constant to $67.8 km/s \cdot Mpc$, considering a flat Universe with the matter density parameter $\Sigma_M = 0.308$ and the vacuum density parameter $\Sigma_{vac} = 0.692$. Taking into account these parameters, the calculation gives $D_L = 355.2 Mpc$. Then I measured the coordinates, declination δ and right ascension RA, of the core, the northern and the southern emission (Table4) on the radio map shown in Figure 15.

I obtained the angular size of the jets calculating the separation between both the emissions and the core. The angular dimension on the approaching jet is $d_1 = 60.6 arcsec$, while the size of the counter jet is $d_2 = 57.8 arcsec$. I obtained the projected size of each emission as the product of their angular size and the scale of $1.487 kpc/''$, given by the cosmological calculator:

$$D_1^S = scale \cdot d_1 = 1.487 \frac{kpc}{''} \cdot 60.6'' = 90.11 \quad kpc \tag{23}$$

REGION	RIGHT ASCENSION RA	DECLINATION δ
Core	03:54:32.853	-13.40.07.244
Southern emission	03:54:32.077	-13.41.08.737
Northern emission	03:54:32.804	-13.39.11.125

Table 4: The equatorial coordinates of the core, the northern and the southern emission

$$D_2^N = scale \cdot d_2 = 1.487 \frac{kpc}{''} \cdot 57.8'' = 85.95 \quad kpc \tag{24}$$

Dividing the projected size of the approaching D_1^S and of the counter jet D_2^N by the sine of the jet inclination θ_1, I obtained the deprojected linear size of both jets:

$$D_{jet1}^{appr} = \frac{D_1^S}{sin(\theta_1)} = \frac{90.11 \quad kpc}{sin(70°)} = 124 \quad kpc \tag{25}$$

$$D_{jet1}^{coun} = \frac{D_2^N}{sin(\theta_1)} = \frac{85.95 \quad kpc}{sin(70°)} = 92 \quad kpc \tag{26}$$

I did the calculations also for the jet inclination θ_2:

$$D_{jet2}^{appr} = \frac{D_1^S}{sin(\theta_2)} = \frac{90.11 \quad kpc}{sin(47°)} = 124 \quad kpc \tag{27}$$

$$D_{jet2}^{coun} = \frac{D_2^N}{sin(\theta_2)} = \frac{85.95 \quad kpc}{sin(47°)} = 118 \quad kpc \tag{28}$$

Since the jets are not aligned it is not possible to calculate the deprojected linear size of the whole jet, for this reason, I summed the two components only to have an estimation of the extension of the emission from north to south:

$$D_{jet1} = D_{jet1}^{approaching} + D_{jet1}^{counter} = 188 kpc \tag{29}$$

And also for the second estimate:

$$D_{jet2} = D_{jet2}^{approaching} + D_{jet2}^{counter} = 242 kpc \tag{30}$$

Until now, the J0354-1340 jet is the most extended jet observed among NLS1s. Usually NLS1s harbour jets of few kpc, so this size is unprecedented for this kind of AGN. The jet is so huge that it is

outside the host, probably reaching the IGM.
In the end, I estimated the age of the approaching jet, considering first that the jet is propagating at 0.99c. Having 1 pc $\approx 3.086 \cdot 10^{13}$km and 1yrs $= 31536 \cdot 10^{3}$s, I calculated the ages as:

$$t = \frac{D_{jet1}^{appr}}{0.99c} = \frac{96 \cdot 3.086 \cdot 10^{16} \quad km}{0.99 \cdot 3 \cdot 10^{5} \quad km/s} \simeq 99.8 \cdot 10^{11} s \simeq 0.3 \quad Myrs \quad (31)$$

Then I consider that the jet is propagating at 0.5c, having:

$$t = \frac{D_{jet2}^{appr}}{0.5c} = \frac{124 \cdot 3.086 \cdot 10^{16} \quad km}{0.5 \cdot 3 \cdot 10^{5} \quad km/s} \simeq 255 \cdot 10^{11} s \simeq 0.8 \quad Myrs \quad (32)$$

The age of the jet of J0354-1340 is of the order of Myrs.

Part III

NEAR-INFRARED ANALYSIS

5 NIR MORPHOLOGY

In this Chapter I will describe the study of the NIR morphology of J0354-1340 host galaxy.

5.1 INTRODUCTION

Galaxy morphology is the result of several factors such as the galaxy formation, the interaction with its environment, the influence of inner perturbations, and the star formation (SF) history (Buta, 2011).
Perturbations generated in the inner part of the galaxy are generally caused by the AGN activity through feedback mechanisms, such as outflows, jets and winds. For this reason, the host galaxy of an AGN interacts and evolves simultaneously with the nuclear region and the host galaxy morphology is linked, in this way, to the central engine activity (Ferrarese and Merritt, 2000, Morganti, 2017). There is a strong connection between the growth of the black hole and the evolution of its galactic surroundings which has been confirmed by several empirical relations (Magorrian et al., 1998) that involve the black hole mass and the bulge properties of its host galaxy. This tight connection between the central engine and the galaxy is also visible in the relation between the relativistic jets and their host, which can be the cause of the suppression or enhancement of SF activity far from the nucleus (Lanz et al., 2016, Morganti, 2017). Further studies have also demonstrated that AGN influence on their hosts is proportional to the jet power (Olguín-Iglesias et al., 2016, Wagner, Bicknell, and Umemura, 2012, Zhuang and Ho, 2020). Even if jets are one of the fundamental components of AGN, the debate on their formation and evolution is still ongoing and the study of host galaxy morphology offer a fresh perspective to solve this problem. Until recently, powerful relativistic radio jets were only found to be hosted in elliptical galaxies (Urry and Padovani, 1995, Franceschini, Vercellone, and Fabian, 1998, Kotilainen, Hyvönen, and Falomo, 2005), formed in dense environments by merging, which is considered the trigger of the jet activity (Chiaberge et al. (2015)).
To investigate the AGN jet phenomenon, the NLS1s class could represent an interesting laboratory. As explained above, NLS1s properties can be interpreted as a sign of early stage of evolution (Mathur, 2000b) or due to a projection effect produced by a pole-one vision (Decarli et al., 2008). Considering that more massive BHs are generally found to be hosted in ellipticals while spiral galaxies tend to harbour less massive BHs, the study of the host galaxy properties of NLS1s could

be useful to disentangle these two scenarios, and to add insights into the launching of jets.

While a large number of non-jetted NLS1 hosts have been already studied (Crenshaw, Kraemer, and Gabel, 2003, Mathur et al., 2012, Krongold, Dultzin-Hacyan, and Marziani, 2001, Orban de Xivry et al., 2011), jetted NLS1s are relatively unexplored (D'Ammando et al., 2018, Antón, Browne, and Marchã, 2008, Berton et al., 2019 Kotilainen et al., 2016, Järvelä, Lähteenmäki, and Berton, 2018b, Olguín-Iglesias et al., 2016, Olguín-Iglesias, Kotilainen, and Chavushyan, 2020). Recently, Järvelä, Lähteenmäki, and Berton (2018b) presented a NIR imaging study with the Nordic Optical Telescope (NOT). All the resolved sources were hosted by late-type galaxies, most with pseudo-bulges and bars, and three of them harbouring powerful relativistic jets. This result gives new evidence supporting the idea that spiral galaxies with pseudo-bulges can launch and sustain powerful jets Olguín-Iglesias, Kotilainen, and Chavushyan, 2020.

Pseudo-bulges are disk-like bulge with flat structures, containing substructures and showing sign of dust obscuration. They are kinematically cold objects, so dinamically supported by the rotation velocity, and they are populated by young stars, showing ongoing star formation. They are thought to be formed via internal secular processes since merger seems to be able to disturb or even destroy the substructures. Pseudo-bulge are found in spiral galaxies. Classical bulge instead, spheroidal featureless structures populated by old stars and kinematically hot, are usually formed as a consequence of merger (Gadotti, Lecture notes). They are usually found in elliptical galaxies.

The high fraction of jetted interacting sources found may suggest that mergers and interaction could play a role in the launching of relativistic jets. In dense group and cluster-scale environments, multiple minor and major mergers can replenish the gas reservoirs and cause gas infall, leading to enhanced star formation and triggering of the AGN activity, or can strip the galaxy of its gas reservoirs, quenching or preventing future star formation. At the same time, as the probability of interaction increases in crowded regions, also the possibility of the launching of jets becomes higher in those environments for NLS1s. This scenario is supported by the discovery that jetted NLS1 galaxies are found in denser large-scale environments than non-jetted NLS1 galaxies (Järvelä et al., 2017, Järvelä, Lähteenmäki, and Berton, 2018b). Nevertheless, different studies do not agree on the results (D'Ammando et al., 2018, D'Ammando et al., 2017) and, for this reason, further studies with a larger sample are required to clarify the situation.

Figure 19: Magellan Telescopes at Las Campanas Observatory, Chile, during observations. Walter Baade telescope is the one to the left and Landon T. Clay telescope is the one to the right. Wikipedia

5.2 DATA SET

The NIR observations of J0354-1340 were carried out during one night, October 10, 2019, with the Magellan Baade 6.5m telescope at Las Campanas Observatory, Chile (Figure 19). These observations were part of a larger project aimed at determining the host galaxy morphologies of NLS1s. The Ks- ($\lambda_{central} = 2.150\mu m$) and J-band ($\lambda_{central} = 1.250\mu m$) observations were performed using the wide-area near-infrared camera FourStar (Figure 20).

The FourStar Infrared Camera has four HAWAII-2RG 2048x2048 detectors and the second Array SN204 in FullWell Mode was used

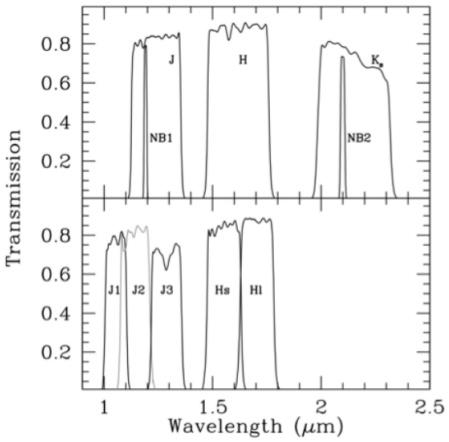

Figure 20: Available filters of the FourStar Camera FourStar Handout

for these observations. The corresponding gain is $2.59e^{-}/ADU$ while the read-out noise is $22.1e^{-}$. The detector scale is $0.159''/pix$. giving a field of view (FoV) of $5.4' \times 5.4'$ per array (FourStar Handout). During the observing night, the sky was clear. The seeing was approximately 0.5" in both bands. There was no need for applying a correction for atmospheric extinction because the airmass was very close to 1 (1.039). The total exposure time was $\approx 1200sec$ (83 frames $\times$ $14.556sec$) and $\approx$ $760sec$ (131 frames $\times$ $5.82sec$), for the J- and Ks-band images, respectively. The seeing was about $0.52arcsec$ and about $0.57arcsec$, for J and Ks images respectively. Standard pre-reduction, photometric and astrometric calibrations, and sky subtraction were applied to the images with the Image Reduction and Analysis Facility (IRAF) Software.

5.3 GALFIT

A way to determine the host galaxy morphology is to characterise its several components for example bulge, disk, bar, ring, and spiral arms, by modelling their light distributions. To study the host galaxy morphology of J0354-1340, I used the 2D fitting algorithm GALFIT version 3.0.5 (GALFIT Home Page), to perform a photometric decomposition of the Ks- and J-band images. GALFIT, is a tool designed to extract structural components from galaxy images and to model brightness profiles using parametric functions. The algorithm can simultaneously fit a galaxy with an arbitrary number of functions, composed of parameters, that can be left free to vary or frozen, and that can be adjusted to model a wide variety of different structures (Peng et al., 2010, Peng et al., 2002).
GALFIT is based on a non-linear least-squares fitting algorithm using the Levenberg-Marquardt technique to find the best solution to a fit. It determines the goodness of fit by calculating the chi-squared χ^2. GALFIT computes the parameters for the next step continuing to iterate until the χ^2 has reached an acceptable value. The goodness of the fit is given by the normalised or reduced chi-squared, the χ^2_ν, defined as :

$$\chi^2_\nu = \frac{1}{N_{dof}} \sum_{x=1}^{nx} \sum_{y=1}^{ny} \frac{(f_{data}(x,y) - f_{model}(x,y))^2}{\sigma(x,y)^2}, \tag{33}$$

where

$$f_{model}(x,y) = \sum_{\nu=1}^{m} f_\nu(x,y;\alpha_1 ... \alpha_n). \tag{34}$$

N_{dof} is the number of degrees of freedom in the fit; nx and ny are the x and y image dimensions; and f_{data}(x,y) is the image flux at

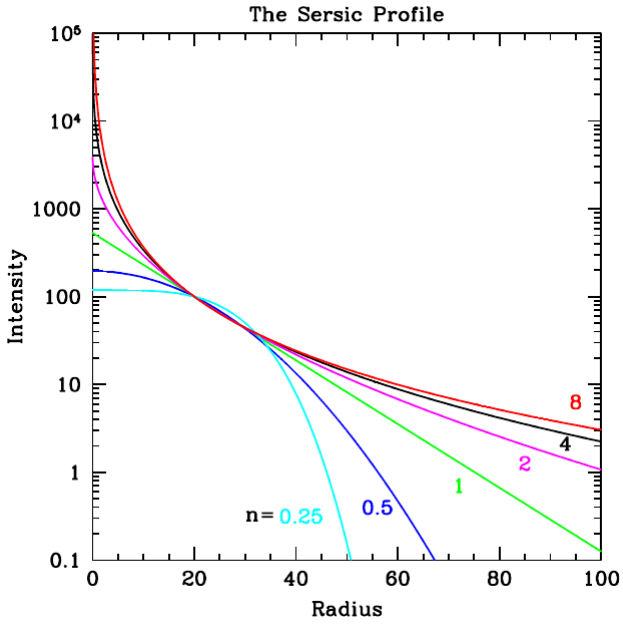

Figure 21: Sérsic profiles with different Sérsic indices where r_e and $\Sigma(r_e)$ are fixed. Larger n_s means steeper central core and more extended outer wing while a lower n_s profile shows a flatter core and a more sharply truncated wing (Peng et al., 2010).

pixel (x, y). The f_{model}(x,y) is the sum of m functions of $f_\nu(x, y; \alpha_1 ... \alpha_n)$ with n free parameters $(\alpha_1 ... \alpha_n)$ in the 2D model. The uncertainty as a function of pixel position, $\sigma(x, y)$, is the Poisson error at each pixel, which can be provided as an input image (Peng et al., 2010, Peng et al., 2002).

5.3.1 *Radial profile*

Several analytic functions are available in GALFIT for fitting light profiles. The radial profile functions describe the model intensity decreasing from the peak. Generally, while early-type galaxies show a steep radial profile in the inner part and extended wings in the outer part, late-type galaxies present a shallower intensity slope in the centre and evident truncation at large radii. Finding the parameters that define the functional form is useful in performing galaxy classification and in investigating the jet/AGN co-evolution. GALFIT provides as radial profile the following functional forms:

- *The Sérsic Profile*
  It is a generalisation of the de Vaucouleurs' law and it describes how the galaxy surface brightness $\Sigma(r)$ varies as a function of the distance r from its centre. The Sérsic power law is one of the

most frequently used functions to model galaxy morphology, and it can be expressed as:

$$\Sigma(r) = \Sigma(r_e) \cdot \exp\left\{-\kappa_{ns}\left[\left(\frac{r}{r_e}\right)^{1/n_s} - 1\right]\right\}. \tag{35}$$

κ_n is a parameter connected to the Sérsic index, n_s, so that $\Sigma(r_e)$ is the surface brightness at r_e. The parameter n_s is the power-law index and it controls the degree of curvature of the profile. When $\Sigma(r_e)$ is plotted against r/r_e and n_s is small, the profile is shallower in the inner part and it has a steep truncation at a large radius. Conversely, when n_s is large, the inner profile is steeper and it shows a highly extended outer wing (Figure 21). The parameter r_e is the effective radius in which half of the total flux is enclosed, and this is due to how the dependent variable κ is coupled to n. Most of the galaxy bulges are fitted by Sérsic profiles with $\frac{1}{2} < n_s < 10$. Usually, bigger and brighter galaxies tend to be fitted with larger n_s. Indeed, the best-fit value of n_s correlates with galaxy size and luminosity. The de Vaucouleurs profile is a special case of the Sérsic function when $n_s = 4$ and it describes elliptical galaxy bulges. Both the exponential and Gaussian functions are also special cases of the Sérsic function when $n_s = 1$ and $n_s = 0.5$ and they are usually used for describing spiral galaxies disk and dwarf elliptical galaxies radial profile and bars. Generally, a Sérsic function with $n_s > 2$ describes classical bulges, as well as ellipticals. Disk-like bulges are better described with Sérsic indices $n_s < 2$, and galaxy disks are described by a Sérsic function with $n_s = 1$ that gives the exponential function (Gadotti, Lecture notes).

- *The Exponential Disk Profile*
  As previously discussed, the exponential disk profile can be expressed as a Sérsic function with $n_=1$:

$$\Sigma(R) = \Sigma_0 \cdot e^{-\frac{r}{r_s}}. \tag{36}$$

  where Σ_0 is the central surface brightness and r_s is the disk scale length. For this profile, the scale length r_s is defined as 1.678 times the effective radius r_e. Usually, disk galaxies are fitted with a central Sérsic component and exponential disk component

- *The Nuker Law*
  It is a good model for fitting most inner 1D profiles of galaxies. The functional form of the Nuker law is defined by a double power law mediated by a smooth transition:

$$I(r) = I_b \cdot 2^{\frac{\beta-\gamma}{\alpha}} \cdot \left(\frac{r}{r_b}\right)^{-\gamma} \cdot \left[1 + \left(\frac{r}{r_b}\right)^{\alpha}\right]^{\frac{\gamma-\beta}{\alpha}}. \tag{37}$$

Considering the limits of large and small radii, the parameter γ is the slope of the inner power-law while β is the slope of the outer power law. The profile changes slope at the break radius r_b, I_b is the surface brightness at that radius, and α describes how sharply the two power laws connect.

- *The Gaussian Profile*
  This profile is describe by the well-known function:

$$\Sigma(R) = \Sigma_0 \cdot e^{-\frac{r^2}{2\sigma^2}} \tag{38}$$

  and the relation between the FWHM and σ is:

$$FWHM = 2\sqrt{2\ln 2} \cdot \sigma \cong 2.355 \cdot \sigma \tag{39}$$

- *The Moffat/Lorentzian Profile*
  The generalized Moffat function has the following form:

$$\Sigma(r) = \frac{\Sigma(0)}{[1 + (r/r_d)^2]^{n_m}}, \tag{40}$$

  where r_d is the dispersion radius and n_m is the power-law index. For $n_m = 1$ The Moffat profile corresponds to a Lorentzian function.

5.3.2 *GALFIT implementation*

To begin the fitting process, GALFIT needs a file.feedme to run (Figure 22). It contains input images, GALFIT control parameters and initial fitting parameters. The four input images are CCD image of the galaxy, and optional input point spread functions (PSF), sigma image, and bad pixel mask. The control parameters are the size of the fitting region and of the convolution box, the magnitude photometric zero-point and the plate scale. The initial fitting parameters depend on the functions chosen to model the galaxy components. The GALFIT fitting process is composed of several steps, as described in the following, and it iterates steps 3-8 until convergence. In some cases, the model does not converge and the iterations stop (Peng et al., 2010, Peng et al., 2002 and *GALFIT user's manual*).

1. The input PSF
   The image of a point source is usually blurred because of distortions due to optics imperfections and Earth's atmosphere turbulence. To compare the intrinsic shape of an object with a model, this effect must be taken into account. This can be done by convolving the model image with the input point spread function (PSF), which is the response of the imaging system to a point source. To create and compare the model with data, first of all,

```
# IMAGE and GALFIT CONTROL PARAMETERS
A) gal.fits            # Input data image (FITS file)
B) imgblock.fits       # Output data image block
C) none                # Sigma image name (made from data if blank or "none")
D) psf.fits   #        # Input PSF image and (optional) diffusion kernel
E) 1                   # PSF fine sampling factor relative to data
F) none                # Bad pixel mask (FITS image or ASCII coord list)
G) none                # File with parameter constraints (ASCII file)
H) 1    200  1    100  # Image region to fit (xmin xmax ymin ymax)
I) 100    100          # Size of the convolution box (x y)
J) 20.000              # Magnitude photometric zeropoint
K) 1.000  1.000        # Plate scale (dx dy)   [arcsec per pixel]
O) both                # Display type (regular, curses, both)
P) 0                   # Choose: 0=optimize, 1=model, 2=imgblock, 3=subcomps

# INITIAL FITTING PARAMETERS
#
#   For component type, the allowed functions are:
#       sersic, expdisk, edgedisk, devauc, king, nuker, psf,
#       gaussian, moffat, ferrer, and sky.
#
#   Hidden parameters will only appear when they're specified:
#       Bn (n=integer, Bending Modes).
#       C0 (diskiness/boxiness),
#       Fn (n=integer, Azimuthal Fourier Modes).
#       R0-R10 (coordinate rotation, for creating spiral structures).
#       To, Ti, T0-T10 (truncation function).
#
# ------------------------------------------------------------------------------
#   par)    par value(s)    fit toggle(s)    # parameter description
# ------------------------------------------------------------------------------

# Component number: 1
 0) sersic3 /              #  Component type
 1) 50.0000  50.0000  1 1  #  Position x, y
 3) 15.0000      1         #  Surface brghtnss @ outer R_break [mag/arcsec^2]
 4) 30.0000      1         #  R_e (effective radius)   [pix]
 5) 4.0000       1         #  Sersic index n (de Vaucouleurs n=4)
 9) 0.7000       1         #  Axis ratio (b/a)
10) -30.0000     1         #  Position angle (PA) [deg: Up=0, Left=90]
Ti)  2                     #  Inner truncation by component number(s)
F5) 0.1500   20.0000  1 1  #  Azim. Fourier mode 5, amplitude, & phase angle

# Component number: 2
T0) radial                 #  Truncation type (radial, length, height)
T1) 45.0000  45.0000  1 1  #  Position x, y
T4) 8.0000       1         #  Break radius (99% normal flux)    [pixels]
T5) 5.0000       1         #  Softening length (1% normal flux) [pixels]
T9) 0.7000       1         #  Axis ratio (optional)
T10) 45.0000     1         #  Position angle (optional) [deg: Up=0, Left=90]
F1) 0.6000   20.0000  1 1  #  Azim. Fourier mode 1, amplitude, & phase angle
B2) -5.000e+00   1         #  Bending mode 2 amplitude

# Component number: 3
 0) sersic                 #  Component type
 1) 150.0000 50.0000  1 1  #  Position x, y
 3) 7.0000       1         #  Integrated magnitude
 4) 15.0000      1         #  R_e (effective radius)   [pix]
 5) 2.0000       1         #  Sersic index n (de Vaucouleurs n=4)
 9) 0.5000       1         #  Axis ratio (b/a)
10) 0.0000       1         #  Position angle (PA) [deg: Up=0, Left=90]

R0) power                  #  PA rotation func. (power, log, none)
R1) 0.0000       1         #  Spiral inner radius [pixels]
R2) 15.0000      1         #  Spiral outer radius [pixels]
R3) 180.0000     1         #  Cumul. rotation out to outer radius [degrees]
R4) 0.3000       1         #  Asymptotic spiral powerlaw
R9) 10.0000      1         #  Inclination to L.o.S. [degrees]
R10) 45.0000     1         #  Sky position angle
F1) 0.3000   45.0000  1 1  #  Azim. Fourier mode 1, amplitude, & phase angle
F5) 0.1000   90.0000  1 1  #  Azim. Fourier mode 5, amplitude, & phase angle
```

Figure 22: Example of a feedme file. It contains input images, control parameters and initial fitting parameters (Peng et al., 2010).

GALFIT normalises the input PSF image for the convolution. The PSF is then Fourier transformed using fast Fourier transform (FFT). To achieve a compromise between the accuracy and the speed of the computation, in GALFIT the user is allowed to decide on the size of the convolution region. The box size should be just big enough so that the seeing does not affect the galaxy profile outside of the box. Typically, the size is about 20 or more times the seeing diameters, depending on how extended the PSF wings are.

2. The extraction of a sub-image
   GALFIT gives the possibility of fitting the entire image or a subregion, which is useful for small objects. In this way, GALFIT cuts out a section of the image centred on the object to fit from the original data image. The user is allowed to choose the size of the fitting region.

3. The creation of model images and derivative images.
   To optimise the galaxy profile parameters, GALFIT uses a downhill gradient method that requires both the model and flux derivative images based on new or initial input parameters.

4. The extraction of the convolution region
   The model and derivative images created are then convolved with the PSF to account for the seeing.

5. Convolve the convolution regions
   The convolution regions removed from the model and derivative images are convolved with the PSF using FFT.

6. Copying the Convolution Region
   The model and derivative images are copied back into the original model/derivative images, once the convolution is done.

7. Minimising residuals
   The process of minimisation, done using the Levenberg-Marquardt expansion, repeats until convergence is achieved, which happens when the χ^2 does not change more than 0.0005 for five iterations. GALFIT can fail to produce a good solution for complicated fit and the convergence cannot be achieved sometimes. GALFIT quits without a solution when tries to fit more components into the image than appropriate or when the power-law indices of the functions are too big or too small.

8. Iteration from step number 3 until convergence is achieved

9. Output images and final parameter files.
   The output image block is a 3-D image cube in FITS. The image data cube has 4 layers. Image zero is blank. The first image is the sub-image extracted. The second image is the final model

of the galaxy in that region. The third image is the residual image formed by subtracting the second from the first. The final parameters obtained in the fit are stored in the FITS header of the second image.

5.4 DATA ANALYSIS AND DISCUSSIONS

In this section, I will present the Ks- and J-band NIR modelling of the host galaxy of J0354-1340 in order to determine its morphology type. I will describe the photometric decomposition performed using the 2D image decomposition algorithm GALFIT.

5.4.1 *Magnitude zero-point*

The magnitude zero-point m_0 is a GALFIT control parameter, and it is used to calculate, together with the exposure time, the magnitude of the surface brightness of the host galaxy model. It is a conversion factor to obtain the calibrated magnitude m_{cal} in physical units, starting from the instrumental magnitude m_s in counts.
To properly model this source, therefore, I calculated the photometric zero-point for J and Ks images. For that purpose, I used the aperture photometry technique, the measurement of the stellar flux within a circular area, whose radius is approximately equal to the FWHM of the stellar PSF.
First of all, I selected eleven bright and non-saturated stars within the FoV, deriving their calibrated magnitudes, in J and Ks bands, from the Two Micron All Sky Survey (2MASS) Catalogue (2MASS Catalog). I used the IRAF task *imexamine* to measure and calculate the mean FWHM value for each star and the mean of the sky standard deviation (Σ_{sky}) for both images. Through the *phot* task, I measured the instrumental magnitude choosing an aperture radius *Rap* of five times the mean FWHM value. The sky was subtracted defining a ring region, the sky annulus, around the aperture with an internal radius *Rann* of seven times the mean FWHM value and a width *Wann* of a quarter of the *Rap*. I also set the CCD readout noise, the CCD gain values and the exposure time for both images (in Table 5 all the parameter values).

In this way, I could calculate the magnitude zero-point for each star, comparing their instrumental magnitudes m_s, measured on the image, with calibrated magnitudes m_{cal} derived from the catalogue. The magnitude zero-point m_0 has indeed the following form:

$$m_0 = m_{cal} - (m_s - ZP) + kX \tag{41}$$

In the equation 41: ZP is the zero point of magnitude scale and it is an arbitrary constant, generally fixed at 25 in order to have positive magnitudes in the calculations; k is the atmospheric extinction

PARAMETER	KS-BAND IMAGE	J-BAND IMAGE
Mean FWHM	3.3 px	3.5 px
Σ_{sky}	4.74 cts/px	3.26 cts/px
Rap	17 px	18px
Rann	25 px	25px
Wann	5 px	6px
Readout noise	22.1 e-/CDR	22.1 e-/DU
Gain	2.59 e-/DU	2.59 e-/DU
Exposure time	5.822 sec	14.555 sec

Table 5: Parameters needed for the calculation of the magnitude zero-point m_0 with the aperture photometry technique, for both Ks- and J-band images.

coefficient while X is the airmass. In this case, the airmass was very close to 1 so I did not take into account the factor kX. I calculated the m_0 for each star and then I obtained the mean, the median and the standard deviation (σ_{sd}) values for both images (Table 6):

PARAMETER	KS-BAND IMAGE	J-BAND IMAGE
Mean	24.8	25.8
Median	24.9	26
Standard deviation	0.53	0.38

Table 6: The mean, the median and the standard deviation σ_{sd} value of m_0 for both images.

The related errors, err_{m_0}, were calculated as the standard error of the mean:

$$err_{m_0} = \frac{\sigma_{sd}}{\sqrt{n}} \tag{42}$$

where n is the number of stars. In this way, choosing the mean value as the reference value for m_0, I obtained:

- For Ks-band : $m_0 = 24.8 \pm 0.16$
- For J-band: $m_0 = 25.8 \pm 0.12$

These values were then used in GALFIT to convert pixel values and fluxes into a physical magnitude by the standard definition (*GALFIT user's manual*):

$$mag = -2.5 log_{10}(\frac{ADUs}{t_{exp}}) + m_0 \tag{43}$$

5.4.2 *PSF*

The nuclear emission coming from the AGN affects the host galaxy model. For this reason, the AGN contamination has to be subtracted from the galaxy before modelling it. This can be done by fitting the AGN component with a modelled PSF. For this purpose, it is possible to use a stellar PSF since also the AGN is also a point-like source. There are several methods to create a stellar PSF.
First of all, I used the PSF photometry technique in IRAF, which models the image PSF using the light distribution of chosen stars. This technique usually replaces the aperture photometry when the stars are not really isolated and/or the field is very crowded. I did several attempts using the *daophot* task: I started creating a stellar PSF with the eleven stars previously selected, but more stars were needed to obtain a good PSF. Then I did the same procedure as before using multiple stars but the PSF obtained was still affected by the distortions in the detector along the FoV. To fix this problem, I modelled the PSF shape as a linear function of the position on the image and I also chose a bigger value for the radius of PSF model (fifteen times the mean FWHM) to see the shape of the stars' wings. This model was still affected by errors due to the field being too crowded. For these reasons, I tried taking the average FWHM of the stars in the image and creating a Gaussian model using GALFIT, and then I used that as the PSF model. The PSF size was indeed too small to let the wings be visible. I did the last attempt in this way trying to fit multiple stars in GALFIT, using identical components (Sérsic functions or a combination of Gaussians plus exponential disks) that differ only in position and magnitude and constraining all the components to have the same parameters. This approach did not work because stars with different brightness had to be fitted with different components.

Finally, I tried using a nearby star as close as possible to the AGN to minimise the effects of the position-dependent PSF. I extracted the isolated star pretty close to the galaxy on its west side from the image (Figure 23), I subtracted the sky contribution within the cut-out region and I used this star as the model PSF itself. This attempt was not optimal since the star was quite faint compared to the AGN. I choose to model the nearby star to obtain an infinite signal-to-noise ratio (S/N), having zero as the value of the sky, to smooth out any tiny imaging errors affecting the star. I fitted the nearby star with one

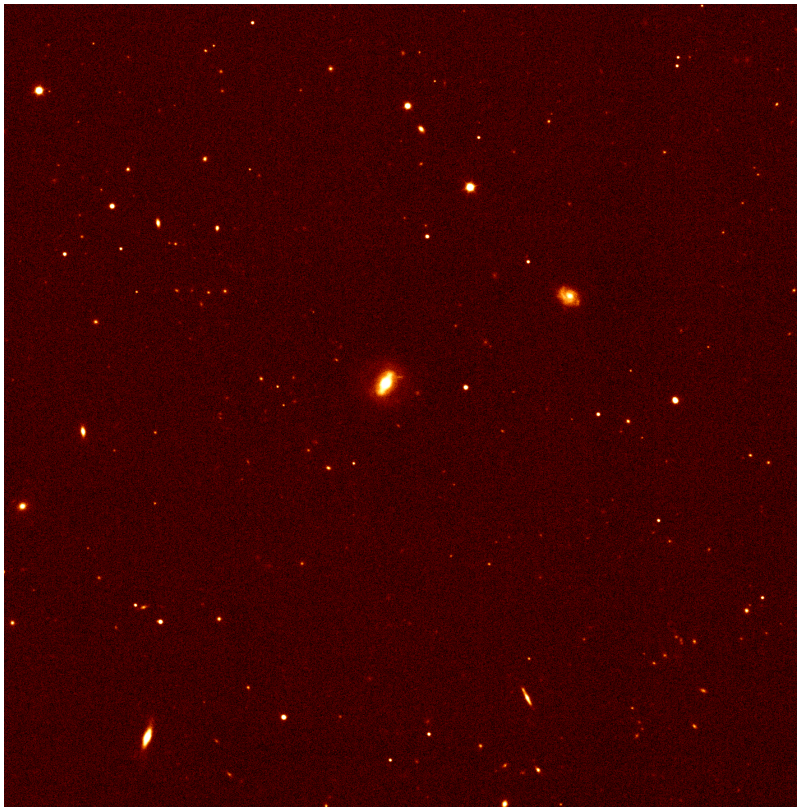

Figure 23: The Ks-band image. The source is at the centre of the FoV and it is possible to see the nearby star close to the galaxy on its right side.

Gaussian in GALFIT but only one function was not enough to properly model the PSF. For this reason, I tried fitting the star in GALFIT with different combinations of Gaussians and exponential disks and extracting the model PSF. The resulting PSF used for the galaxy fit did not give a proper model for the host galaxy. Finally, I obtained the best PSF model fitting five Sérsic functions for the nearby star, freezing the sky mean value to zero in the fit.

5.4.3 *Galaxy modelling with GALFIT*

I performed a photometric decomposition of the Ks-band image using GALFIT. A crucial part of the fitting, as previously explained, was to properly model the PSF to remove the AGN contamination. The galaxy sky background was estimated using IRAF. I measured the sky in several different isolated regions within the FoV and I fixed the mean value (0.2) in the fitting. The magnitude photometric zero-point m_0=24.8 and the plate scale value 0.160 were added in the file.feedme as GALFIT control parameters. I selected a fitting region size of 300 $\times$ 300 pixels, centred on the AGN, as large as possible to contain only the source. I chose a convolution box size of 200 pixels.
I made several attempts to properly fit the host galaxy. I first used the PSF model only to fit the nuclear component and checked the residuals to see if additional components were needed. Then, I added three Sersìc functions, convolved with the PSF, for the bulge, the disk and the bar component respectively. I tried to model the host galaxy using different PSF models, as described in the previous section. At each step, I varied the initial fitting parameters to make sure that the output parameter values were stable, and I also varied the number of components until the best fit was achieved. The main problem in the fitting procedure was that often some of the output parameters were not physically meaningful (e.g., the Sersìc index of the bulge was either close to zero or $\approx$ 20 , depending on the initial parameters) and the residuals showed a ring-like structure around the centre, especially enhanced at the 'poles' of the bar (Figure 24). This could be an effect of the PSF on the galaxy fit, especially when the stellar wings were not included in the model. Sometimes, the fit also reached the maximum number of iterations before converging.

Using the PSF model of the nearby star fit with five Sersìc functions I was able to obtain the best galaxy fit. I kept all the parameters free to have as unbiased a fit as possible. The goodness of fit was determined based on the χ^2_ν value, 1.271, and the accordance between the input and the output parameters, which remains physical and stable during the fit. The presence of some additional light sources in the fitting region may have affected the fit, resulting in a higher χ^2_ν.
The sky is the largest source of error in the fit and in addition, there

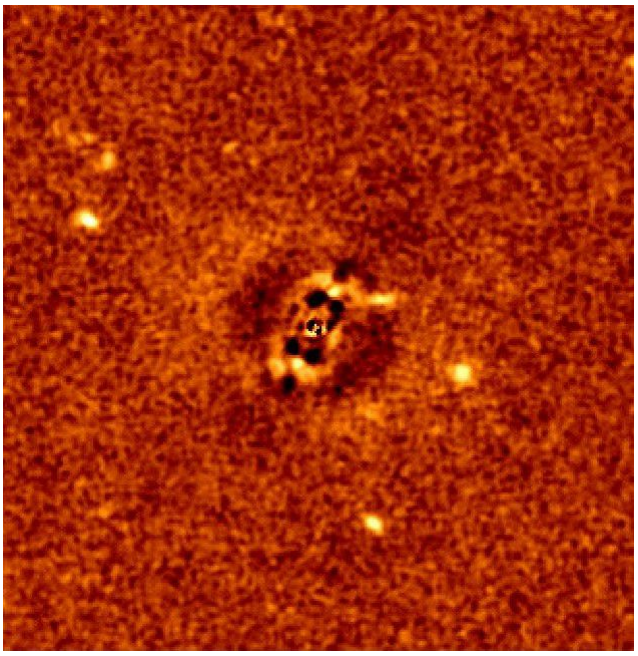

Figure 24: Central region of the residuals image, showing the dark ring around the nuclear region and the peculiar bar. For this fit, I have modelled the AGN component with a PSF function and three Sérsic functions for the bulge, the disk and the bar. I let all the parameters vary freely, which clearly resulted in a bulge/bar/disk morphology with a reduced χ^2_ν of 1.247.

are two sources of error for the magnitude: the error related to the zero point calculation and the error given by the 2MASS Catalogue. I calculated the sky standard error of the mean σ_{sky} as the ratio between the mean sky standard deviation Σ_{sky} and the root mean square of the number of the sky measurements n:

$$\sigma_{sky} = \frac{\Sigma_{sky}}{\sqrt{n}} = \frac{4.74}{\sqrt{11}} = 1.43 \tag{44}$$

To obtain the errors for all the parameters of each component, except the magnitude, I fitted the galaxy adding and then subtracting the σ_{sky} to the sky mean value. In this way, I calculated the differences between the best fit value of each parameter and the two other values obtained changing the sky. I did the same for the χ^2_ν. I also converted r_e values from pixel to kpc, assuming that at the distance of the galaxy (D = 355.2Mpc), one pixel corresponds to (1.487kpc/″) kpc. The magnitude error is made up of three components: the err_{m_0}, the error derived from the 2MASS catalogue and the error from GALFIT err_{gal}. I calculated the standard error of the mean for the values of magnitude obtained from the 2MASS catalogue as:

$$\sigma_{2MASS} = \frac{\Sigma_{2MASS}}{\sqrt{n}} = \frac{1.15}{\sqrt{11}} = 0.35 \tag{45}$$

Finally, for each component, I summed in quadrature the three sources of error, taking into the account the GALFIT errors separately, as following:

$$err_{mag} = \sqrt{err^2_{m_0} + sigma^2_{2MASS} + err^2_{gal}} \quad (46)$$

The output parameters of the best fit are shown in Table 7.

component	mag	r_e (kpc)	n	axial ratio	PA (°)	NOTES
PSF	$14.29^{+0.39}_{-0.42}$					
Sérsic 1	$14.06^{+0.40}_{-0.55}$	$1.15^{+0.12}_{-0.75}$	$4.24^{+0.74}_{-2.03}$	$0.91^{+0.00}_{-0.00}$	$-45.81^{+0.56}_{-5.41}$	bulge
Sérsic 2	$13.72^{+0.42}_{-0.40}$	$8.63^{+0.79}_{-2.89}$	$0.56^{+0.08}_{-2.01}$	$0.83^{+0.04}_{-0.07}$	$-38.94^{+1.69}_{-0.06}$	disk
Sérsic 3	$14.51^{+0.39}_{-0.60}$	$4.40^{+0.08}_{-0.33}$	$0.37^{+0.01}_{-0.12}$	$0.33^{+0.01}_{-0.06}$	$-28.24^{+0.02}_{-0.89}$	bar

Table 7: Best fit parameters of J0354-1340 with χ^2_ν=$1.271^{+0.09}_{-0.00}$

The best fit was achieved with four components: one PSF and three Sérsic functions. The nuclear component was fitted with the PSF, while the bulge, the disk, and the bar were fitted with Sérsic 1, Sérsic 2 and Sérsic 3 respectively. I mainly used the Sérsic profile to model the various components of the source because, simply by changing the Sérsic index n, different galaxy light distribution can be modelled. Sérsic 1 component with $r_e = 1.15$kpc represents the bulge. As previous explained, $n = 4$ gives the traditional de Vaucouleurs profile, used to model the classical bulge. In this case, the Sérsic index of the bulge, $n = 4.24$, is not entirely reliable because the fit is very sensitive to the sky. Smaller values of n are associated with disk-like galaxies and pseudo-bulge, and since it is clear from the images that J0354-1340 is a spiral galaxy, it is expected the bulge Sersìc index to be ≈ 2. The bulge component shows an axial ratio of 0.91.
Sérsic 2 parameters fit those of the disk with the largest effective radius, with respect to the other components, of $r_e = 8.63$kpc, and with $n = 0.56$. Also in this case the Sèrsic index should be closer to 1 to better reproduce the disk. The axial ratio of the disk component is 0.83. Sérsic 3 is a bar-like component with $r_e = 4.40$kpc, $n = 0.37$ and axial ratio of 0.33.

The observed, model and residual image are shown in Figure (25, 26 and 27.

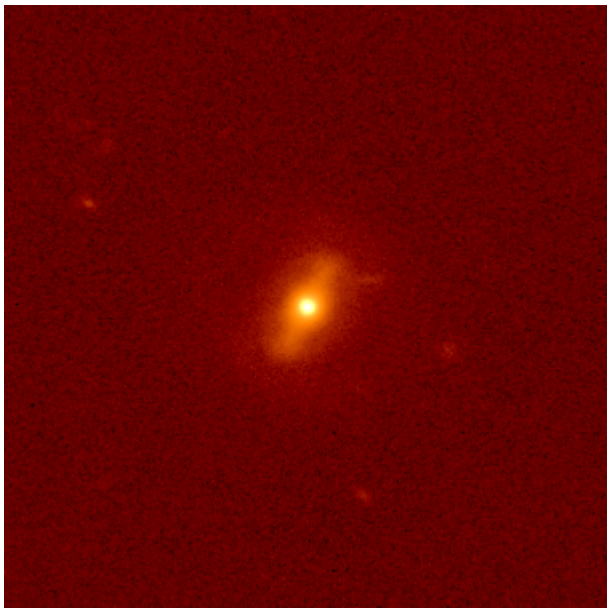

Figure 25: This observed image, which size is the one of the fitting region. It is possible to see the blobs in this image that could have affected the fit.

Figure 26: The model image of the galaxy.

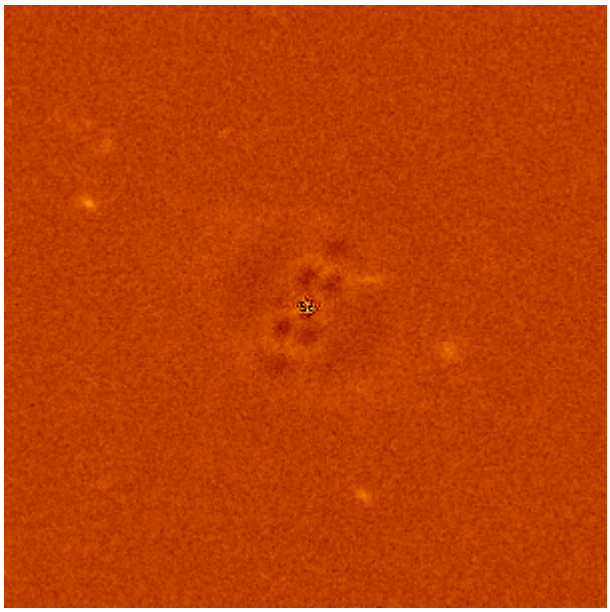

Figure 27: The residual image showing a soft dark ring around the centre and a peculiar bar-like structure. The centre shows both over subtracted and under subtracted regions.

Part IV

CONCLUSIONS

6

CONCLUSIONS

In this thesis, I studied the radio properties of J0354-1340, a peculiar jetted NLS1. This radio source is part of the sample of the southern NLS1s studied in Chen et al., 2020, and it was observed with the JVLA C-configuration at 5.5GHz. It is probably an FRII radio galaxy, classified as RQ by Chen et al., 2020, with $R = S_{5.5\,GHz}/S_{4440\,Å} = 5.6$. I used the multi-term multi-frequency synthesis method implemented in CASA to obtain the radio map, the tapered map and the spectral index map of this source. This NLS1 shows a compact central core bright at radio frequencies and two regions of extended emission, located on the southwest side and on the northeast side of the central region, as seen in the radio map. These regions correspond to the approaching jet, that is the brightest one pointing toward our line of sight, and the receding jet, that is fainter than the previous one, respectively.

In agreement with the debated unreliability of radio loudness (Järvelä et al., 2017, Padovani, 2017), the presence of very elongated jets in this RQ source is not unexpected. NLS1s showing strong radio emission have indeed been observed not necessarily harbouring jets (Gu et al., 2015 Caccianiga et al., 2015) and, on the other hand, some radio-silent NLS1s have recently been detected at 37 GHz, confirming the presence of jets in them (Lähteenmäki et al., 2018). Evidence against the strict division to radio-loud and radio-quiet sources were firstly highlighted by Ho and Peng, 2001, that found RL Sy1, previously classified as RQ sources, measuring the flux densities from the nuclear region only. Then, other proves supporting this theory started to accumulate. The variability seen in AGN (Gabányi et al., 2018), and also the variability due to the changes in the relativistic jets (Foschini et al., 2015), for example, have to be considered affecting the radio loudness parameter *R*.

The peculiarity of this source is due to the size of the extended emission. The projected linear sizes of a hundred kpc of the radio lobes are consistent with those of FRII radio galaxies (Hardcastle et al., 1998, Kharb et al., 2008). J0354-1340 harbours indeed the largest radio jets found to date in an NLS1, that usually show sizes of the order of tens of kpc (Doi et al., 2012, Congiu et al., 2017, Gabányi et al., 2018, Richards and Lister, 2015).

Until now, the largest known projected size of the lobe separation among NLS1 radio sources was of 116kpc, found by Rakshit et al., 2018. The projected linear size of the whole extended emission of this source is instead about 200kpc. This estimate does really not repre-

sent the size of the whole jet, since the jets are not aligned, as seen in the radio map. Furthermore, the measure of the extension of the emission from north to south depends on the jet velocity and so on the inclination, chosen for the calculations.

Using an approximation for β of 0.99, the obtained jet inclination, $\theta_1 = 70°$, is much higher than a few dozen degrees, generally obtained for kpc scale jetted NLS1 galaxies (Doi et al., 2012, Rakshit et al., 2018, Richards and Lister, 2015). Considering also that NLS1s are generally observed at low viewing angle, the measured value for the inclination is very unusual for this kind of object. This is probably due to the fact that the approximation of $v_{jet} = 0.99c$ is not realistic, since the jet propagates at speeds much lower than the speed of light. It is also worth noting that the fluxes were measured from the hot spots in the ends of each jet and not from the actual jets, giving a less reliable measurement. A more reasonable approximation could be $\beta = 0.5$, giving an inclination on $\theta_2 = 47°$, which is consistent with the range of viewing angles for NLS1s. This value does not imply a face-on view of the nucleus. Taking into account this estimate, the deprojected size of the whole extended emission is about 242kpc. The jet is so huge that it propagates outside the host galaxy (Morganti et al., 2015). Jets have been observed interacting with the interstellar medium, disturbing the kinematics of the NLR gas (Komossa et al., 2008, Berton et al., 2016). On the other end, a dense circumnuclear and interstellar medium could hamper the propagation of relativistic jets due to its interaction with the cloud (van Breugel, Miley, and Heckman, 1984), clearly not the case of this source. The age of the approaching jet estimated using the approximation of $\beta = 0.5$ gives a lower limit for the age of $\approx 8 \times 10^5$ years. This lies at the low tail of the age range of 10^5 to 10^7 years found for other RL NLS1s (Doi et al., 2012, Richards and Lister, 2015, Rakshit et al., 2018.

Considering the spectral index map, the compact core, which may represent the jet base, shows a flat in-band spectral index, as in blazars. The spectral index of the extended emission, ≈ -0.5, is slightly larger than the usual spectral index of ≈ -0.7 of optically thin synchrotron emission. This can be caused by the interaction between the jets and the ISM, producing the flattening of the spectral index.

Since the supermassive BH interacts and co-evolves with its closest environment, the host galaxy morphology is linked to the central engine activity (Kormendy and Ho, 2013). This has been confirmed by several empirical relations that involve the BH mass and the bulge features of its host galaxy (Magorrian et al., 1998). Generally, more massive BHs are found to be hosted in elliptical galaxies while spiral galaxies tend to harbour less massive BH (Salucci et al., 2000). Until now, only a few studies have focused on NLS1 hosts, finding that these AGN are preferably, but not only, hosted in disk-like galaxies, often with pseudo-bulges and bars (Järvelä, Lähteenmäki, and Berton,

2018b).
For this work, I also studied the host galaxy morphology of J0354-1340, performing the Ks and J band NIR imaging. The NIR observations of J0354-1340 were carried out with the Magellan Baade 6.5m Telescope, using the wide-area NIR camera FourStar. I used the 2D image decomposition algorithm GALFIT to perform a photometric decomposition of the images to determine the morphological type of the host galaxy. To remove the AGN contamination from the galaxy, I fitted the nuclear region of the host galaxy with a modelled stellar PSF. The best galaxy fit was achieved with three Sérsic functions corresponding respectively to the bulge, the disk and the bar. The goodness of fit was determined based on the reduced χ^2_ν value of 1.271. From the photometric decomposition performed on this object, J0354-1340 is hosted in a barred spiral galaxy, probably with a pseudo-bulge. This proved that relativistic jets can be harboured also in spirals. Until recently, only a few jetted NLS1s have been studied individually (D'Ammando et al., 2018, Berton et al., 2019, Kotilainen et al., 2016, Järvelä, Lähteenmäki, and Berton, 2018a, Olguín-Iglesias, Kotilainen, and Chavushyan, 2020), and generally, but not in all cases, they were found hosted by late-type galaxies. Usually, most powerful relativistic jets have been associated with the highly evolved massive elliptical galaxies with considerably higher BH masses, formed in dense environments (Urry and Padovani, 1995, Kotilainen, Hyvönen, and Falomo, 2005). These galaxies undergo the phase of the formation of jets, that coincides with the formation of the classical bulge, probably via merger induced (Kormendy and Gebhardt, 2001, Urry, 2003). In spiral galaxies, secular processes, rather than interaction and mergers, dominate the bulge-growth, the BH activity and the formation of pseudo-bulges. Nevertheless, spiral galaxies have been found to host kpc-scale or even Mpc-scale relativistic jets (Hota et al., 2011).
J0354-1340 lies in this scenario, an RQ source harbouring the largest radio jets found to date in an NLS1, hosted in a disk-like galaxy with a pseudo-bulge. The black hole mass of J0354-1340 found by Chen et al. (2020) was of $\log(M_{BH}M_\odot) \approx 6.99$. In this way, these results confirm the validity of the low-mass scenario, for which NLS1s represent the young evolutionary phase of AGN (Mathur, 2000a).

BIBLIOGRAPHY

ATNF. *Resolution and sensitivity*. URL: https://www.atnf.csiro.au/outreach/education/senior/astrophysics/resolution_sensitivity.html.

Alison Peck Jim Braatz, Ashley Bemis. *Introduction to Radio Interferometry*. https://science.nrao.edu/facilities/alma/naasc-workshops/nrao-cd-fit/BasicsInterf.pdf.

Antón, S., I. W. A. Browne, and M. J. Marchã (Nov. 2008). "The colour of the narrow line Sy1-blazar 0324+3410." In: *aap* 490.2, pp. 583–587. DOI: 10.1051/0004-6361:20078926. arXiv: 0907.2400 [astro-ph.GA].

Antonucci, Robert (Jan. 1993). "Unified models for active galactic nuclei and quasars." In: *araa* 31, pp. 473–521. DOI: 10.1146/annurev.aa.31.090193.002353.

Baade, W. and R. Minkowski (1982). "1954, Identification of the Radio Sources in Cassiopeia, Cygnus A and Puppis A." In: *Classics in Radio Astronomy*. Vol. 10, p. 251. DOI: 10.1007/978-94-009-7752-5_29.

Beckmann, Volker and Chris R. Shrader (2012). *Active Galactic Nuclei*. Provided by the SAO/NASA Astrophysics Data System. URL: https://ui.adsabs.harvard.edu/abs/2012agn..book.....B.

Berton, M., L. Foschini, S. Ciroi, V. Cracco, G. La Mura, F. Di Mille, and P. Rafanelli (June 2016). "[O III] line properties in two samples of radio-emitting narrow-line Seyfert 1 galaxies." In: *aap* 591, A88, A88. DOI: 10.1051/0004-6361/201527056. arXiv: 1506.05800 [astro-ph.GA].

Berton, M., E. Järvelä, L. Crepaldi, A. Lähteenmäki, M. Tornikoski, E. Congiu, P. Kharb, G. Terreran, and A. Vietri (Apr. 2020). "Absorbed relativistic jets in radio-quiet narrow-line Seyfert 1 galaxies." In: *aap* 636, A64, A64. DOI: 10.1051/0004-6361/202037793. arXiv: 2003.02654 [astro-ph.GA].

Berton, M. et al. (June 2018). "Radio-emitting narrow-line Seyfert 1 galaxies in the JVLA perspective." In: *aap* 614, A87, A87. DOI: 10.1051/0004-6361/201832612. arXiv: 1801.03519 [astro-ph.GA].

Berton, M. et al. (Feb. 2019). "The Interacting Late-type Host Galaxy of the Radio-loud Narrow-line Seyfert 1 IRAS 20181-2244." In: *aj* 157.2, 48, p. 48. DOI: 10.3847/1538-3881/aaf5ca. arXiv: 1807.08953 [astro-ph.GA].

Best, P. N. and T. M. Heckman (Apr. 2012). "On the fundamental dichotomy in the local radio-AGN population: accretion, evolution and host galaxy properties." In: *mnras* 421.2, pp. 1569–1582. DOI: 10.1111/j.1365-2966.2012.20414.x. arXiv: 1201.2397 [astro-ph.CO].

Blandford, R. D. and R. L. Znajek (May 1977). "Electromagnetic extraction of energy from Kerr black holes." In: *mnras* 179, pp. 433–456. DOI: 10.1093/mnras/179.3.433.

Boller, Th. (Jan. 2000). "X-Ray Observations of Agn." In: *New Vistas in Astrophysics*. Ed. by Maurice M. Shapiro, Rein Silberberg, Todor S. Stanev, and John P. Wefel, p. 143.

Boroson, Todd A. and Richard F. Green (May 1992). "The Emission-Line Properties of Low-Redshift Quasi-stellar Objects." In: *apjs* 80, p. 109. DOI: 10.1086/191661.

Buta, Ronald J. (Feb. 2011). "Galaxy Morphology." In: *arXiv e-prints*, arXiv:1102.0550, arXiv:1102.0550. arXiv: 1102.0550 [astro-ph.CO].

Caccianiga, A., S. Antón, L. Ballo, L. Foschini, T. Maccacaro, R. Della Ceca, P. Severgnini, M. J. Marchã, S. Mateos, and E. Sani (Aug. 2015). "WISE colours and star formation in the host galaxies of radio-loud narrow-line Seyfert 1." In: *mnras* 451.2, pp. 1795–1805. DOI: 10.1093/mnras/stv939. arXiv: 1504.07068 [astro-ph.GA].

Carniani, Stefano (2012). MA thesis. University of Florence.

Chen, S. et al. (Aug. 2020). "Radio morphology of southern narrow-line Seyfert 1 galaxies with Very Large Array observations." In: *mnras* 498.1, pp. 1278–1297. DOI: 10.1093/mnras/staa2373. arXiv: 2006.01700 [astro-ph.GA].

Chiaberge, Marco, Roberto Gilli, Jennifer M. Lotz, and Colin Norman (June 2015). "Radio Loud AGNs are Mergers." In: *apj* 806.2, 147, p. 147. DOI: 10.1088/0004-637X/806/2/147. arXiv: 1505.07419 [astro-ph.GA].

Condon, James J. and Scott M. Ransom (2016). *Essential Radio Astronomy*.

Congiu, E. et al. (July 2017). "Kiloparsec-scale emission in the narrow-line Seyfert 1 galaxy Mrk 783." In: *aap* 603, A32, A32. DOI: 10.1051/0004-6361/201730616. arXiv: 1704.03881 [astro-ph.GA].

Cracco, V., S. Ciroi, M. Berton, F. Di Mille, L. Foschini, G. La Mura, and P. Rafanelli (Oct. 2016). "A spectroscopic analysis of a sample of narrow-line Seyfert 1 galaxies selected from the Sloan Digital Sky Survey." In: *mnras* 462.2, pp. 1256–1280. DOI: 10.1093/mnras/stw1689. arXiv: 1607.03438 [astro-ph.GA].

Cracco, V., S. Ciroi, F. di Mille, L. Vaona, A. Frassati, A. A. Smirnova, G. La Mura, A. V. Moiseev, and P. Rafanelli (Dec. 2011). "The origin of gas in extended narrow-line regions of nearby Seyfert galaxies - I. NGC 7212." In: *mnras* 418.4, pp. 2630–2641. DOI: 10.1111/j.1365-2966.2011.19654.x. arXiv: 1109.1195 [astro-ph.CO].

Crenshaw, D. M., S. B. Kraemer, and J. R. Gabel (Oct. 2003). "The Host Galaxies of Narrow-Line Seyfert 1 Galaxies: Evidence for Bar-Driven Fueling." In: *aj* 126.4, pp. 1690–1698. DOI: 10.1086/377625. arXiv: astro-ph/0306404 [astro-ph].

D'Ammando, F., J. A. Acosta-Pulido, A. Capetti, R. D. Baldi, M. Orienti, C. M. Raiteri, and C. Ramos Almeida (July 2018). "The host

galaxy of the γ-ray-emitting narrow-line Seyfert 1 galaxy PKS 1502+036." In: *mnras* 478.1, pp. L66–L71. DOI: 10.1093/mnrasl/sly072. arXiv: 1804.10220 [astro-ph.GA].

D'Ammando, F., J. A. Acosta-Pulido, A. Capetti, C. M. Raiteri, R. D. Baldi, M. Orienti, and C. Ramos Almeida (July 2017). "Uncovering the host galaxy of the ensuremathgamma-ray-emitting narrow-line Seyfert 1 galaxy FBQS J1644+2619." In: *mnras* 469.1, pp. L11–L15. DOI: 10.1093/mnrasl/slx042. arXiv: 1703.07367 [astro-ph.GA].

Decarli, Roberto, Massimo Dotti, Marcella Fontana, and Francesco Haardt (May 2008). "Are the black hole masses in narrow-line Seyfert 1 galaxies actually small?" In: *mnras* 386.1, pp. L15–L19. DOI: 10.1111/j.1745-3933.2008.00451.x. arXiv: 0801.4560 [astro-ph].

Doi, Akihiro, Hiroshi Nagira, Nozomu Kawakatu, Motoki Kino, Hiroshi Nagai, and Keiichi Asada (Nov. 2012). "Kiloparsec-scale Radio Structures in Narrow-line Seyfert 1 Galaxies." In: *apj* 760.1, 41, p. 41. DOI: 10.1088/0004-637X/760/1/41. arXiv: 1210.1303 [astro-ph.GA].

Fanaroff, B. L. and J. M. Riley (May 1974). "The morphology of extragalactic radio sources of high and low luminosity." In: *mnras* 167, 31P–36P. DOI: 10.1093/mnras/167.1.31P.

Fath, Edward Arthur (Jan. 1909). "The spectra of some spiral nebulae and globular star clusters." In: *Lick Observatory Bulletin* 149, pp. 71–77. DOI: 10.5479/ADS/bib/1909LicOB.5.71F.

Ferrarese, Laura and David Merritt (Aug. 2000). "A Fundamental Relation between Supermassive Black Holes and Their Host Galaxies." In: *apjl* 539.1, pp. L9–L12. DOI: 10.1086/312838. arXiv: astro-ph/0006053 [astro-ph].

Foschini, L. et al. (Mar. 2015). "Properties of flat-spectrum radio-loud narrow-line Seyfert 1 galaxies." In: *aap* 575, A13, A13. DOI: 10.1051/0004-6361/201424972.

Franceschini, A., S. Vercellone, and A. C. Fabian (July 1998). "Supermassive Black Holes in Early-Type Galaxies: Relationship with Radio Emission and Constraints on the Black Hole Mass Function." In: *mnras* 297.3, pp. 817–824. DOI: 10.1046/j.1365-8711.1998.01534.x. arXiv: astro-ph/9801129 [astro-ph].

Gabányi, K. É., S. Frey, Z. Paragi, E. Järvelä, T. Morokuma, T. An, M. Tanaka, and I. Tar (Jan. 2018). "The radio structure of the peculiar narrow-line Seyfert 1 galaxy candidate J1100+4421." In: *mnras* 473.2, pp. 1554–1561. DOI: 10.1093/mnras/stx2449. arXiv: 1709.07202 [astro-ph.GA].

Gary, Prof. Dale E. *Primary Antenna Elements*. URL: https://web.njit.edu/~gary/728/Lecture4.html.

Giommi, P., P. Padovani, G. Polenta, S. Turriziani, V. D'Elia, and S. Piranomonte (Mar. 2012). "A simplified view of blazars: clearing

the fog around long-standing selection effects." In: *mnras* 420.4, pp. 2899–2911. DOI: 10.1111/j.1365-2966.2011.20044.x. arXiv: 1110.4706 [astro-ph.CO].

Giroletti, M. and A. Polatidis (Feb. 2009). "Samples and statistics of CSS and GPS sources." In: *Astronomische Nachrichten* 330.2, p. 193. DOI: 10.1002/asna.200811154. arXiv: 0904.1068 [astro-ph.CO].

Goodrich, Robert W. (July 1989). "Spectropolarimetry of "Narrow-Line" Seyfert 1 Galaxies." In: *apj* 342, p. 224. DOI: 10.1086/167586.

Greenstein, Jesse L. and Maarten Schmidt (July 1964). "The Quasi-Stellar Radio Sources 3C 48 and 3C 273." In: *apj* 140, p. 1. DOI: 10.1086/147889.

Gu, Minfeng, Yongjun Chen, S. Komossa, Weimin Yuan, Zhiqiang Shen, Kiyoaki Wajima, Hongyan Zhou, and J. A. Zensus (Nov. 2015). "The Radio Properties of Radio-loud Narrow-line Seyfert 1 Galaxies on Parsec Scales." In: *apjs* 221.1, 3, p. 3. DOI: 10.1088/0067-0049/221/1/3. arXiv: 1509.01889 [astro-ph.GA].

Hardcastle, M. J., P. Alexander, G. G. Pooley, and J. M. Riley (May 1998). "FRII radio galaxies with z<0.3 - I. Properties of jets, cores and hotspots." In: *mnras* 296.2, pp. 445–462. DOI: 10.1046/j.1365-8711.1998.01480.x. arXiv: astro-ph/9801179 [astro-ph].

Heckman, Timothy M. and Philip N. Best (Aug. 2014). "The Coevolution of Galaxies and Supermassive Black Holes: Insights from Surveys of the Contemporary Universe." In: *araa* 52, pp. 589–660. DOI: 10.1146/annurev-astro-081913-035722. arXiv: 1403.4620 [astro-ph.GA].

Ho, Luis C. and Chien Y. Peng (July 2001). "Nuclear Luminosities and Radio Loudness of Seyfert Nuclei." In: *apj* 555.2, pp. 650–662. DOI: 10.1086/321524. arXiv: astro-ph/0102502 [astro-ph].

Hota, Ananda, S. K. Sirothia, Youichi Ohyama, C. Konar, Suk Kim, Soo-Chang Rey, D. J. Saikia, J. H. Croston, and Satoki Matsushita (Oct. 2011). "Discovery of a spiral-host episodic radio galaxy." In: *mnras* 417.1, pp. L36–L40. DOI: 10.1111/j.1745-3933.2011.01115.x. arXiv: 1107.4742 [astro-ph.CO].

Hubble, E. P. (Dec. 1926). "Extragalactic nebulae." In: *apj* 64, pp. 321–369. DOI: 10.1086/143018.

Isella, Andrea. *Interferometry basics*. https://science.nrao.edu/opportunities/courses/casa-caltech-winter2012/Isella_Radio_Interferometry_Basics_Caltech2012.pdf.

Jaeger, S. (Aug. 2008). "The Common Astronomy Software Application (CASA)." In: *Astronomical Data Analysis Software and Systems XVII*. Ed. by R. W. Argyle, P. S. Bunclark, and J. R. Lewis. Vol. 394. Astronomical Society of the Pacific Conference Series, p. 623.

Järvelä, E., A. Lähteenmäki, and M. Berton (Apr. 2018a). "Host galaxies of jetted narrow-line Seyfert 1 galaxies." In: *Revisiting Narrow-Line Seyfert 1 Galaxies and their Place in the Universe*, p. 46.

Järvelä, E., A. Lähteenmäki, and M. Berton (Nov. 2018b). "Near-infrared morphologies of the host galaxies of narrow-line Seyfert 1 galaxies." In: *aap* 619, A69, A69. DOI: 10.1051/0004-6361/201832876. arXiv: 1807.02970 [astro-ph.GA].

Järvelä, E., A. Lähteenmäki, H. Lietzen, A. Poudel, P. Heinämäki, and M. Einasto (Sept. 2017). "Large-scale environments of narrow-line Seyfert 1 galaxies." In: *aap* 606, A9, A9. DOI: 10.1051/0004-6361/201731318. arXiv: 1707.01411 [astro-ph.GA].

Kellermann, K. I., R. Sramek, M. Schmidt, D. B. Shaffer, and R. Green (Oct. 1989). "VLA Observations of Objects in the Palomar Bright Quasar Survey." In: *aj* 98, p. 1195. DOI: 10.1086/115207.

Khachikian, E. Y. and D. W. Weedman (Sept. 1974). "An atlas of Seyfert galaxies." In: *apj* 192, pp. 581–589. DOI: 10.1086/153093.

Kharb, P., C. P. O'Dea, S. A. Baum, R. A. Daly, M. P. Mory, M. Donahue, and E. J. Guerra (Jan. 2008). "A Study of 13 Powerful Classical Double Radio Galaxies." In: *apjs* 174.1, pp. 74–110. DOI: 10.1086/520840. arXiv: astro-ph/0702009 [astro-ph].

Komossa, S., D. Xu, H. Zhou, T. Storchi-Bergmann, and L. Binette (June 2008). "On the Nature of Seyfert Galaxies with High [O III] λ5007 Blueshifts." In: *apj* 680.2, pp. 926–938. DOI: 10.1086/587932. arXiv: 0803.0240 [astro-ph].

Komossa, Stefanie, Wolfgang Voges, Dawei Xu, Smita Mathur, Hans-Martin Adorf, Gerard Lemson, Wolfgang J. Duschl, and Dirk Grupe (Aug. 2006). "Radio-loud Narrow-Line Type 1 Quasars." In: *aj* 132.2, pp. 531–545. DOI: 10.1086/505043. arXiv: astro-ph/0603680 [astro-ph].

Kormendy, John and Karl Gebhardt (Oct. 2001). "Supermassive black holes in galactic nuclei." In: *20th Texas Symposium on relativistic astrophysics*. Ed. by J. Craig Wheeler and Hugo Martel. Vol. 586. American Institute of Physics Conference Series, pp. 363–381. DOI: 10.1063/1.1419581. arXiv: astro-ph/0105230 [astro-ph].

Kormendy, John and Luis C. Ho (Aug. 2013). "Coevolution (Or Not) of Supermassive Black Holes and Host Galaxies." In: *araa* 51.1, pp. 511–653. DOI: 10.1146/annurev-astro-082708-101811. arXiv: 1304.7762 [astro-ph.CO].

Kotilainen, J. K., T. Hyvönen, and R. Falomo (Sept. 2005). "The luminous host galaxies of high redshift BL Lac objects." In: *aap* 440.3, pp. 831–843. DOI: 10.1051/0004-6361:20042548. arXiv: astro-ph/0505443 [astro-ph].

Kotilainen, Jari K., Jonathan León-Tavares, Alejandro Olguín-Iglesias, Maarten Baes, Christopher Anórve, Vahram Chavushyan, and Luis Carrasco (Dec. 2016). "Discovery of a Pseudobulge Galaxy Launching Powerful Relativistic Jets." In: *apj* 832.2, 157, p. 157. DOI: 10.3847/0004-637X/832/2/157. arXiv: 1609.02417 [astro-ph.GA].

Krongold, Y., D. Dultzin-Hacyan, and P. Marziani (Feb. 2001). "Host Galaxies and Circumgalactic Environment of "Narrow Line" Seyfert 1 Nuclei." In: *aj* 121.2, pp. 702–709. DOI: 10.1086/318768.

Lähteenmäki, A., E. Järvelä, V. Ramakrishnan, M. Tornikoski, J. Tammi, R. J. C. Vera, and W. Chamani (June 2018). "Radio jets and gamma-ray emission in radio-silent narrow-line Seyfert 1 galaxies." In: *aap* 614, L1, p. L1. DOI: 10.1051/0004-6361/201833378. arXiv: 1806.02058 [astro-ph.GA].

Lanz, Lauranne, Patrick M. Ogle, Katherine Alatalo, and Philip N. Appleton (July 2016). "Star Formation Suppression Due to Jet Feedback in Radio Galaxies with Shocked Warm Molecular Gas." In: *apj* 826.1, 29, p. 29. DOI: 10.3847/0004-637X/826/1/29. arXiv: 1511.05968 [astro-ph.GA].

Leipski, C., H. Falcke, N. Bennert, and S. Hüttemeister (Aug. 2006). "The radio structure of radio-quiet quasars." In: *aap* 455.1, pp. 161–172. DOI: 10.1051/0004-6361:20054311. arXiv: astro-ph/0606540 [astro-ph].

Lynden-Bell, D. (May 1964). "On Large-Scale Instabilities during Gravitational Collapse and the Evolution of Shrinking Maclaurin Spheroids." In: *apj* 139, p. 1195. DOI: 10.1086/147860.

Magorrian, John et al. (June 1998). "The Demography of Massive Dark Objects in Galaxy Centers." In: *aj* 115.6, pp. 2285–2305. DOI: 10.1086/300353. arXiv: astro-ph/9708072 [astro-ph].

Mathur, Smita (June 2000a). "Narrow-line Seyfert 1 galaxies and the evolution of galaxies and active galaxies." In: *mnras* 314.4, pp. L17–L20. DOI: 10.1046/j.1365-8711.2000.03530.x. arXiv: astro-ph/0003111 [astro-ph].

Mathur, Smita (June 2000b). "Narrow-line Seyfert 1 galaxies and the evolution of galaxies and active galaxies." In: *mnras* 314.4, pp. L17–L20. DOI: 10.1046/j.1365-8711.2000.03530.x. arXiv: astro-ph/0003111 [astro-ph].

Mathur, Smita, Dale Fields, Bradley M. Peterson, and Dirk Grupe (Aug. 2012). "Supermassive Black Holes, Pseudobulges, and the Narrow-line Seyfert 1 Galaxies." In: *apj* 754.2, 146, p. 146. DOI: 10.1088/0004-637X/754/2/146. arXiv: 1102.0537 [astro-ph.CO].

Mineshige, Shin, Toshihiro Kawaguchi, Mitsuru Takeuchi, and Kiyoshi Hayashida (June 2000). "Slim-Disk Model for Soft X-Ray Excess and Variability of Narrow-Line Seyfert 1 Galaxies." In: *pasj* 52, pp. 499–508. DOI: 10.1093/pasj/52.3.499. arXiv: astro-ph/0003017 [astro-ph].

Morganti, R., T. A. Oosterloo, J. B. R. Oonk, W. Frieswijk, and C. N. Tadhunter (Dec. 2015). "Radio Jets Clearing the Way Through a Galaxy: Watching Feedback in Action in the Seyfert Galaxy IC 5063." In: *Revolution in Astronomy with ALMA: The Third Year*. Ed. by D. Iono, K. Tatematsu, A. Wootten, and L. Testi. Vol. 499. As-

tronomical Society of the Pacific Conference Series, p. 125. arXiv: 1504.04694 [astro-ph.GA].

Morganti, Raffaella (Nov. 2017). "The many routes to AGN feedback." In: *Frontiers in Astronomy and Space Sciences* 4, 42, p. 42. DOI: 10.3389/fspas.2017.00042. arXiv: 1712.05301 [astro-ph.GA].

NRAO. *CASA*. URL: https://casa.nrao.edu/.

NRAO. *Introduction to Imaging in CASA*. https://science.nrao.edu/facilities/alma/naasc-workshops/nrao-cd-wvu17/Intro_CASA_Imaging.pdf.

NRAO. *Synthesis Calibration*. URL: https://casa.nrao.edu/casadocs/casa-6.1.0/calibration-and-visibility-data/synthesis-calibration/introduction.

NRAO. *VLA Self-calibration Tutorial*. URL: https://casaguides.nrao.edu/index.php?title=VLA_Self-calibration_Tutorial-CASA5.7.0.

NRAO. *Very Large Array*. URL: https://public.nrao.edu/telescopes/vla/.

NRAO/AUI/NSF. *The National Science Foundation's Jansky Very Large Array*. URL: https://public.nrao.edu/news/2018-nine-mappp/.

Narayan, Ramesh and Insu Yi (June 1994). "Advection-dominated Accretion: A Self-similar Solution." In: *apjl* 428, p. L13. DOI: 10.1086/187381. arXiv: astro-ph/9403052 [astro-ph].

Olguín-Iglesias, A., J. León-Tavares, J. K. Kotilainen, V. Chavushyan, M. Tornikoski, E. Valtaoja, C. Añorve, J. Valdés, and L. Carrasco (Aug. 2016). "The host galaxies of active galactic nuclei with powerful relativistic jets." In: *mnras* 460.3, pp. 3202–3220. DOI: 10.1093/mnras/stw1208. arXiv: 1605.05525 [astro-ph.GA].

Olguín-Iglesias, Alejandro, Jari Kotilainen, and Vahram Chavushyan (Feb. 2020). "The disc-like host galaxies of radio-loud narrow-line Seyfert 1s." In: *mnras* 492.1, pp. 1450–1464. DOI: 10.1093/mnras/stz3549. arXiv: 1912.02746 [astro-ph.GA].

Orban de Xivry, G., R. Davies, M. Schartmann, S. Komossa, A. Marconi, E. Hicks, H. Engel, and L. Tacconi (Jan. 2011). "Past and present secular evolution in the host galaxies of NLS1s." In: *Narrow-Line Seyfert 1 Galaxies and their Place in the Universe*. Ed. by L. Foschini, M. Colpi, L. Gallo, D. Grupe, S. Komossa, K. Leighly, and S. Mathur, p. 36.

Osterbrock, D. E. and R. W. Pogge (Oct. 1985). "The spectra of narrow-line Seyfert 1 galaxies." In: *apj* 297, pp. 166–176. DOI: 10.1086/163513.

Osterbrock, Donald E. and Gary J. Ferland (2006). *Astrophysics of gaseous nebulae and active galactic nuclei*. Provided by the SAO/NASA Astrophysics Data System. URL: https://ui.adsabs.harvard.edu/abs/2006agna.book.....O.

Padovani, Paolo (Aug. 2017). "On the two main classes of active galactic nuclei." In: *Nature Astronomy* 1, 0194, p. 0194. DOI: 10.1038/s41550-017-0194. arXiv: 1707.08069 [astro-ph.GA].

Peck, Alison. *Introduction to radio interferometry*. National Radio Astronomy Observatory.

Peng, Chien Y. *GALFIT user's manual*. For Galfit 3.0.4 and more recent versions.

Peng, Chien Y., Luis C. Ho, Chris D. Impey, and Hans-Walter Rix (July 2002). "Detailed Structural Decomposition of Galaxy Images." In: *aj* 124.1, pp. 266–293. DOI: 10.1086/340952. arXiv: astro-ph/0204182 [astro-ph].

Peng, Chien Y., Luis C. Ho, Chris D. Impey, and Hans-Walter Rix (June 2010). "Detailed Decomposition of Galaxy Images. II. Beyond Axisymmetric Models." In: *aj* 139.6, pp. 2097–2129. DOI: 10.1088/0004-6256/139/6/2097. arXiv: 0912.0731 [astro-ph.CO].

Peterson, B. M. (Jan. 2011). "Masses of Black Holes in Active Galactic Nuclei: Implications for Narrow-Line Seyfert 1 Galaxies." In: *Narrow-Line Seyfert 1 Galaxies and their Place in the Universe*. Ed. by L. Foschini, M. Colpi, L. Gallo, D. Grupe, S. Komossa, K. Leighly, and S. Mathur, p. 32.

Pogge, R. W. (Jan. 2011). "A quarter century of Narrow-Line Sefert 1s." In: *Narrow-Line Seyfert 1 Galaxies and their Place in the Universe*. Ed. by L. Foschini, M. Colpi, L. Gallo, D. Grupe, S. Komossa, K. Leighly, and S. Mathur, p. 2.

Rakshit, Suvendu, C. S. Stalin, Ananda Hota, and Chiranjib Konar (Dec. 2018). "Rare Finding of a 100 Kpc Large, Double-lobed Radio Galaxy Hosted in the Narrow-line Seyfert 1 Galaxy SDSS J103024.95+551622.7." In: *apj* 869.2, 173, p. 173. DOI: 10.3847/1538-4357/aaefe8. arXiv: 1811.02147 [astro-ph.GA].

Rau, U. and T. J. Cornwell (Aug. 2011). "A multi-scale multi-frequency deconvolution algorithm for synthesis imaging in radio interferometry." In: *aap* 532, A71, A71. DOI: 10.1051/0004-6361/201117104. arXiv: 1106.2745 [astro-ph.IM].

Reber, Grote (Nov. 1944). "Cosmic Static." In: *apj* 100, p. 279. DOI: 10.1086/144668.

Richards, Joseph L. and Matthew L. Lister (2015). "KILOPARSEC-SCALE JETS IN THREE RADIO-LOUD NARROW-LINE SEYFERT 1 GALAXIES." In: *The Astrophysical Journal* 800.1, p. L8. ISSN: 2041-8213. DOI: 10.1088/2041-8205/800/1/l8. URL: http://dx.doi.org/10.1088/2041-8205/800/1/L8.

Richstone, D. O. and M. Schmidt (Jan. 1980). "The spectral properties of a large sample of quasars." In: *apj* 235, pp. 361–376. DOI: 10.1086/157640.

Salpeter, E. E. (Aug. 1964). "Accretion of Interstellar Matter by Massive Objects." In: *apj* 140, pp. 796–800. DOI: 10.1086/147973.

Salucci, Paolo, Ewa Szuszkiewicz, Pierluigi Monaco, and Luigi Danese (Jan. 2000). "Erratum: Mass function of dormant black holes and the evolution of active galactic nuclei." In: *mnras* 311.2, pp. 448–448. DOI: 10.1046/j.1365-8711.2000.03091.x.

Sandage, Allan (Jan. 1964). "Intensity Variations of 3C 48, 3C 196, and 3C 273 in Optical Wavelengths." In: *apj* 139, pp. 416–419. DOI: 10.1086/147769.

Sandage, Allan, Philippe Véron, and John D. Wyndham (Oct. 1965). "Optical Identification of New Quasi-Stellar Radio Sources." In: *apj* 142, pp. 1307–1311. DOI: 10.1086/148415.

Sani, E., D. Lutz, G. Risaliti, H. Netzer, L. C. Gallo, B. Trakhtenbrot, E. Sturm, and T. Boller (Apr. 2010). "Enhanced star formation in narrow-line Seyfert 1 active galactic nuclei revealed by Spitzer." In: *mnras* 403.3, pp. 1246–1260. DOI: 10.1111/j.1365-2966.2009.16217.x. arXiv: 0908.0280 [astro-ph.CO].

Savolainen, Tuomas. *Introduction to radio interferometry*. ELE and Metsähovi Radio Observatory.

Schmidt, M. (Mar. 1963). "3C 273 : A Star-Like Object with Large Red-Shift." In: *nat* 197.4872, p. 1040. DOI: 10.1038/1971040a0.

Schmidt, M. and R. F. Green (June 1983). "Quasar evolution derived from the Palomar bright quasar survey and other complete quasar surveys." In: *apj* 269, pp. 352–374. DOI: 10.1086/161048.

Seyfert, Carl K. (Jan. 1943). "Nuclear Emission in Spiral Nebulae." In: *apj* 97, p. 28. DOI: 10.1086/144488.

Shakura, N. I. and R. A. Sunyaev (June 1976). "A theory of the instability of disk accretion on to black holes and the variability of binary X-ray sources, galactic nuclei and quasars." In: *mnras* 175, pp. 613–632. DOI: 10.1093/mnras/175.3.613.

Slipher, V. M. (Jan. 1917). "The spectrum and velocity of the nebula N.G.C. 1068 (M 77)." In: *Lowell Observatory Bulletin* 3, pp. 59–62.

Thompson, A. Richard, James M. Moran, and Jr. Swenson George W. (2017). *Interferometry and Synthesis in Radio Astronomy, 3rd Edition*. DOI: 10.1007/978-3-319-44431-4.

Urry, C. Megan and Paolo Padovani (Sept. 1995). "Unified Schemes for Radio-Loud Active Galactic Nuclei." In: *pasp* 107, p. 803. DOI: 10.1086/133630. arXiv: astro-ph/9506063 [astro-ph].

Urry, M. (Jan. 2003). "The AGN Paradigm for Radio-Loud Objects." In: *Active Galactic Nuclei: From Central Engine to Host Galaxy*. Ed. by Suzy Collin, Francoise Combes, and Isaac Shlosman. Vol. 290. Astronomical Society of the Pacific Conference Series, p. 3. arXiv: astro-ph/0301309 [astro-ph].

Vagnetti, F., E. Giallongo, and A. Cavaliere (Feb. 1991). "BL Lacertae Objects and Radio-loud Quasars within an Evolutionary Unified Scheme." In: *apj* 368, p. 366. DOI: 10.1086/169700.

Wagner, A. Y., G. V. Bicknell, and M. Umemura (Oct. 2012). "Driving Outflows with Relativistic Jets and the Dependence of Active

Galactic Nucleus Feedback Efficiency on Interstellar Medium Inhomogeneity." In: *apj* 757.2, 136, p. 136. DOI: 10.1088/0004-637X/757/2/136. arXiv: 1205.0542 [astro-ph.CO].

West, Jennifer. *Single Dish Astronomy*. https://www.atnf.csiro.au/research/radio-school/2017/lectures/west-single-dish-astronomy-2017.pdf.

Wilson, A. S. and E. J. M. Colbert (May 1995). "The Origin of Powerful Radio Sources." In: *American Astronomical Society Meeting Abstracts #186*. Vol. 186. American Astronomical Society Meeting Abstracts, p. 15.02.

Woltjer, L. (Feb. 1964). "A Source of Energy for Radio Galaxies." In: *nat* 201.4921, pp. 803–804. DOI: 10.1038/201803a0.

Zel'dovich, Ya. B. and I. D. Novikov (Oct. 1964). "The Radiation of Gravity Waves by Bodies Moving in the Field of a Collapsing Star." In: *Soviet Physics Doklady* 9, p. 246.

Zhuang, Ming-Yang and Luis C. Ho (June 2020). "The Interplay between Star Formation and Black Hole Accretion in Nearby Active Galaxies." In: *apj* 896.2, 108, p. 108. DOI: 10.3847/1538-4357/ab8f2e. arXiv: 2007.11283 [astro-ph.GA].

van Breugel, W., G. Miley, and T. Heckman (Jan. 1984). "Studies of kiloparsec-scale, steep-spectrum radio cores. I. VLA maps." In: *aj* 89, pp. 5–22. DOI: 10.1086/113480.